Article:

Shi, P orcid.org/0000-0001-5782-245X, Angus, D orcid.org/0000-0003-0734-7835, Nowacki, A orcid.org/0000-0001-7669-7383 et al. (2 more authors) (2018) Microseismic Full Waveform Modeling in Anisotropic Media with Moment Tensor Implementation. Surveys in Geophysics, 39 (4). pp. 567-611. ISSN 0169-3298

https://doi.org/10.1007/s10712-018-9466-2

Surveys in Geophysics manuscript No.
(will be inserted by the editor)

Microseismic full waveform modeling in anisotropic media with moment tensor implementation

Peidong Shi · Doug Angus · Andy Nowacki · Sanyi Yuan · Yanyan Wang

Received: date / Accepted: date

Abstract Seismic anisotropy is common in the subsurface, especially in shale and fractured rocks. Seismic anisotropy will cause travel-time and amplitude discrepancy

Peidong Shi
School of Earth and Environment, University of Leeds, Leeds, UK
Tel.: +4407761833640
E-mail: eepsh@leeds.ac.uk

Doug Angus (✉)
ESG Solutions, Kingston, Canada
Tel.: +16135488287 ext. 270
E-mail: d.angus@leeds.ac.uk

Andy Nowacki
School of Earth and Environment, University of Leeds, Leeds, UK

Sanyi Yuan
College of Geophysics and Information Engineering, China University of Petroleum, Beijing, China

Yanyan Wang
Department of Earth Sciences, ETH Zurich, Zurich, Switzerland

in different propagation directions. For microseismic monitoring which is often implemented in shale or fractured rocks, seismic anisotropy is an non-negligible influence factor. We developed an efficient finite-difference full waveform modeling tool with arbitrary moment tensor source. The modeling tool is suitable for simulating wave propagation in anisotropic media for microseismic monitoring. As both dislocation and non-double-couple source are often observed in microseismic monitoring, an arbitrary moment tensor source is implemented in the forward modeling tool. We equally distribute the increments of shear stress on the staggered-grid to obtain an accurate and symmetric moment tensor source. Our modeling tool provides an efficient way to obtain the Green's function in anisotropic media, which is the key of anisotropic moment tensor inversion and source mechanism characterization in microseismic monitoring. Seismic anisotropy will make the recorded wavefield more complex and distort the amplitudes and arrival-times of the P- and S-waves, thus making microseismic imaging difficult. Retrieve the anisotropy from microseismic data is very helpful for characterizing the stimulated fracture properties. In our research, wavefields in anisotropic media have been carefully simulated and analysed in both surface array and downhole array. The variation characteristics of travel-time and amplitude of direct P- and S-wave in vertical transverse isotropic media and horizontal transverse isotropic media are distinct, thus providing a feasible way to distinguish and identify the anisotropic type of the subsurface. Analysing the travel-times and amplitudes of the microseismic data is a feasible way to estimate the orientation and density of the induced cracks in hydraulic fracturing.

Keywords Microseismic · Forward modeling · Seismic anisotropy · Moment tensor

1 Introduction

Full waveform modeling (FWM) can help us understand elastic wave propagation in complex media and is widely used in reverse time migration, full waveform inversion and seismic source imaging (Baysal et al 1983; Boyd 2006; Virieux and Operto 2009; Xuan and Sava 2010; Yuan et al 2014). There are two ways to calculate the full waveform solution in an elastic media: analytical solutions and numerical simulation. Analytical solutions, such as Green's function in an infinite half-space medium (Aki and Richards 2002), are mostly used in simple models such as homogeneous or layered media. Numerical solutions, such as finite-difference method (Kelly et al 1976), finite-element method (Zienkiewicz et al 1977) and spectral element method (Tromp et al 2008), are more suitable for modeling wave phenomena in complex media, but are computationally more expensive.

In microseismic monitoring, FWM has been used as a reverse time modeling tool to locate the microseismic source using full waveform data (Gajewski and Tessmer 2005; Steiner et al 2008; Artman et al 2010; O'Brien et al 2011; Saenger et al 2011; Nakata and Beroza 2016). This method does not depend on arrival-time picking, thus can be used on data with low signal-to-noise ratio. FWM is also used as a tool to generate and analyse the often complex full wavefield of microseismic data (Brzak et al 2009; Jin et al 2013; Li et al 2015), to help improve the quality of microseismic imaging. The Green's function of the subsurface can be obtained through FWM, which is critical for source mechanism characterization (Vavryčuk 2007; Kawakatsu and Montagner 2008; Song and Toksöz 2011; Li et al 2011; Chambers et al 2014; Linzer et al 2015). However microseismic monitoring has placed stringent demands on FWM (Hobro et al 2016). Compared with seismic data in conventional reflection seismology and global seismology, microseismic data have relatively high dominant frequency, which can have a significant influence on the character of the wavefield and waveforms (Usher et al 2013; Angus et al 2014). For a reliable source mechanism characterization, this requires FWM with high-precision both in space and time domain. In both natural earthquakes and induced earthquakes (e.g. microseismicity), both double-couple sources and non-double-couple sources are observed (Šílenỳ et al 2009). Thus the moment tensor source representation is appropriate to describe the source mechanism. Modeling different types of sources requires obtaining highly accurate Green's function to understanding the source mechanisms of microseismic event.

Strong seismic anisotropy is often observed in shale and reservoirs which contain lots of natural and/or induced fractures (Johnston and Christensen 1995; Schoenberg and Sayers 1995; Vernik and Liu 1997; Wang 2002; Wang et al 2007; Yan et al 2016). Seismic anisotropy can have a significant influence on the recorded wavefields (both in travel-time and amplitude), thus affecting the results of microseismic interpretation (Warpinski et al 2009). Without considering seismic anisotropy, both source location and mechanism inversion could be biased. The location error induced by seismic anisotropy is also related to the recording geometries of microseismic monitoring (Warpinski et al 2009). Rössler et al (2004) and Vavryčuk (2005) demonstrate that moment tensors for pure-shear sources will generally exhibit significant non-double-couple components in anisotropic media. Their studies show anisotropy can have a significant influence on the interpretation of the source mechanisms. Stierle et al

(2016) demonstrate that the retrieve of moment tensor and source mechanism critically depend on anisotropy using laboratory acoustic emission experiments. Their study also shows that the tensile events are more sensitive to P-wave anisotropy than shear events. For source mechanism characterization, the P- and T-axes of the moment tensors are affected by velocity anisotropy and deviated form the true orientation of faulting (Stierle et al 2016). Understanding and correcting for wave propagation phenomena in anisotropic media will help to reduce uncertainties in source location and mechanism inversion. Grechka and Yaskevich (2013a) demonstrated that the travel-times of microseismic events can provide sufficient information to constrain both locations of microseismic events and the underlying anisotropic velocity model. They use the shear-wave splitting to improve the precision of event locations and locate events whose P-wave time picks are unavailable. A correct analysis of the source mechanism is also achievable through anisotropic moment tensor inversion (Rössler et al 2004). Seismic anisotropy can be retrieved from the recorded microseismic data (Al-Harrasi et al 2011; Zhang et al 2013). For a reliable estimation of seismic anisotropy, a wide aperture of recording array is normally required (Grechka and Yaskevich 2013b). Furthermore seismic anisotropy attributes can also provide more information about the fractured media. Hydraulic fracturing can cause time-lapse changes in the anisotropy parameters. Grechka et al (2011) find the time-lapse changes in the anisotropy parameters rather than velocity heterogeneity need to be introduced to explain the microseismic data recorded at different fracturing stage. The time-lapse changes in the anisotropy parameters can be used to characterize the stimulated reservoir volume or crustal stress variation in cracked rock (Teanby et al

2004). The crack properties such as orientation and density can be studied using seismic anisotropy (Verdon et al 2009; Wuestefeld et al 2010).

Among the FWM methods, the finite-difference (FD) approach is increasingly used because of its ability in modeling complex media and high accuracy. We developed an efficient FWM tool based on FD method, which is suitable for anisotropic media and arbitrary moment tensors. First, we describe the elastodynamic equations in anisotropic media and the special way to implement an accurate and symmetrical moment tensor source in the staggered grid. Then we compared the modeling results of a general moment tensor source with analytical solutions in homogeneous medium to confirm the correctness of this method. Because the far-field approximations are often used in microseismic monitoring, the magnitude of near-field components and far-field components are also compared and discussed in detail in the paper. In the modeling examples part, the wave propagation phenomena are simulated and discussed in both anisotropic layered model and 3-dimensional (3D) anisotropic overthrust model. And the influence of seismic anisotropy on microseismic data are simulated and analysed in detail both for surface and downhole arrays. We examine the feasibility of utilizing recorded microseismic data to estimate seismic anisotropy of the subsurface.

2 Theory

In this section, we present the elastodynamic equations in velocity-stress formation, moment-tensor source representation for the wavefield excitation and the numerical implementation of the elastodynamic equations.

2.1 Elastic wave equation in inhomogeneous and anisotropic media

In 3D Cartesian coordinate system, the equations of momentum conservation are given by

$$
\begin{aligned}
\rho\frac{\partial v_x}{\partial t} &= \frac{\partial \tau_{xx}}{\partial x} + \frac{\partial \tau_{xy}}{\partial y} + \frac{\partial \tau_{xz}}{\partial z},\\
\rho\frac{\partial v_y}{\partial t} &= \frac{\partial \tau_{xy}}{\partial x} + \frac{\partial \tau_{yy}}{\partial y} + \frac{\partial \tau_{yz}}{\partial z},\\
\rho\frac{\partial v_z}{\partial t} &= \frac{\partial \tau_{xz}}{\partial x} + \frac{\partial \tau_{yz}}{\partial y} + \frac{\partial \tau_{zz}}{\partial z}.
\end{aligned}
\tag{1}
$$

After some transformation, the stress-strain relations can be expressed as

$$
\begin{aligned}
\frac{\partial \tau_{xx}}{\partial t} &= c_{11}\frac{\partial v_x}{\partial x} + c_{12}\frac{\partial v_y}{\partial y} + c_{13}\frac{\partial v_z}{\partial z} + c_{14}\left(\frac{\partial v_y}{\partial z} + \frac{\partial v_z}{\partial y}\right)\\
&\quad + c_{15}\left(\frac{\partial v_x}{\partial z} + \frac{\partial v_z}{\partial x}\right) + c_{16}\left(\frac{\partial v_x}{\partial y} + \frac{\partial v_y}{\partial x}\right),\\
\frac{\partial \tau_{yy}}{\partial t} &= c_{21}\frac{\partial v_x}{\partial x} + c_{22}\frac{\partial v_y}{\partial y} + c_{23}\frac{\partial v_z}{\partial z} + c_{24}\left(\frac{\partial v_y}{\partial z} + \frac{\partial v_z}{\partial y}\right)\\
&\quad + c_{25}\left(\frac{\partial v_x}{\partial z} + \frac{\partial v_z}{\partial x}\right) + c_{26}\left(\frac{\partial v_x}{\partial y} + \frac{\partial v_y}{\partial x}\right),\\
\frac{\partial \tau_{zz}}{\partial t} &= c_{31}\frac{\partial v_x}{\partial x} + c_{32}\frac{\partial v_y}{\partial y} + c_{33}\frac{\partial v_z}{\partial z} + c_{34}\left(\frac{\partial v_y}{\partial z} + \frac{\partial v_z}{\partial y}\right)\\
&\quad + c_{35}\left(\frac{\partial v_x}{\partial z} + \frac{\partial v_z}{\partial x}\right) + c_{36}\left(\frac{\partial v_x}{\partial y} + \frac{\partial v_y}{\partial x}\right),\\
\frac{\partial \tau_{yz}}{\partial t} &= c_{41}\frac{\partial v_x}{\partial x} + c_{42}\frac{\partial v_y}{\partial y} + c_{43}\frac{\partial v_z}{\partial z} + c_{44}\left(\frac{\partial v_y}{\partial z} + \frac{\partial v_z}{\partial y}\right)\\
&\quad + c_{45}\left(\frac{\partial v_x}{\partial z} + \frac{\partial v_z}{\partial x}\right) + c_{46}\left(\frac{\partial v_x}{\partial y} + \frac{\partial v_y}{\partial x}\right),\\
\frac{\partial \tau_{xz}}{\partial t} &= c_{51}\frac{\partial v_x}{\partial x} + c_{52}\frac{\partial v_y}{\partial y} + c_{53}\frac{\partial v_z}{\partial z} + c_{54}\left(\frac{\partial v_y}{\partial z} + \frac{\partial v_z}{\partial y}\right)\\
&\quad + c_{55}\left(\frac{\partial v_x}{\partial z} + \frac{\partial v_z}{\partial x}\right) + c_{56}\left(\frac{\partial v_x}{\partial y} + \frac{\partial v_y}{\partial x}\right),\\
\frac{\partial \tau_{xy}}{\partial t} &= c_{61}\frac{\partial v_x}{\partial x} + c_{62}\frac{\partial v_y}{\partial y} + c_{63}\frac{\partial v_z}{\partial z} + c_{64}\left(\frac{\partial v_y}{\partial z} + \frac{\partial v_z}{\partial y}\right)\\
&\quad + c_{65}\left(\frac{\partial v_x}{\partial z} + \frac{\partial v_z}{\partial x}\right) + c_{66}\left(\frac{\partial v_x}{\partial y} + \frac{\partial v_y}{\partial x}\right).
\end{aligned}
\tag{2}
$$

In these equations, (v_x, v_y, v_z) represent the particle velocity components along x-, y- and z-directions respectively and $(\tau_{xx}, \tau_{yy}, \tau_{zz}, \tau_{yz}, \tau_{xz}, \tau_{xy})$ are the components of the stress tensor. The media is characterized by the elastic tensor c_{IJ} and density ρ. Here the fourth-order elastic tensor c_{ijkl} is expressed in Voigt notation (c_{IJ}). Because of symmetry, the elastic tensor has only 21 independent parameters in a general anisotropic medium (Sheriff and Geldart 1995). However the number of independent parameters can be further reduced if the symmetry system of the medium is higher than that of a general anisotropic media. For an isotropic media which is commonly used in seismic modeling and has the highest symmetry system, there are only 2 independent elastic parameters. For vertical transverse isotropic (VTI) and horizontal transverse isotropic (HTI) media, there are 5 independent elastic parameters (Thomsen 1986; Rüger 1997). For tilted transverse isotropic (TTI) and orthorhombic media, there are 9 independent elastic parameters (Tsvankin 1997). For monoclinic media, there are 13 independent elastic parameters (Sayers 1998). When modeling in medium with lower symmetry system, the memory cost will increase greatly. Table 1 shows the comparison of memory costs in different symmetry systems. In a specific media whose symmetry system is higher than or equal to that of orthorhombic media (e.g. orthorhombic, HTI, VTI and isotropic media), the elastic tensor has the same null components. Thus the stress-strain relations can be further simplified as

$$\begin{aligned}
\frac{\partial \tau_{xx}}{\partial t} &= c_{11}\frac{\partial v_x}{\partial x} + c_{12}\frac{\partial v_y}{\partial y} + c_{13}\frac{\partial v_z}{\partial z},\\
\frac{\partial \tau_{yy}}{\partial t} &= c_{21}\frac{\partial v_x}{\partial x} + c_{22}\frac{\partial v_y}{\partial y} + c_{23}\frac{\partial v_z}{\partial z},\\
\frac{\partial \tau_{zz}}{\partial t} &= c_{31}\frac{\partial v_x}{\partial x} + c_{32}\frac{\partial v_y}{\partial y} + c_{33}\frac{\partial v_z}{\partial z},\\
\frac{\partial \tau_{yz}}{\partial t} &= c_{44}\left(\frac{\partial v_y}{\partial z} + \frac{\partial v_z}{\partial y}\right),\\
\frac{\partial \tau_{xz}}{\partial t} &= c_{55}\left(\frac{\partial v_x}{\partial z} + \frac{\partial v_z}{\partial x}\right),\\
\frac{\partial \tau_{xy}}{\partial t} &= c_{66}\left(\frac{\partial v_x}{\partial y} + \frac{\partial v_y}{\partial x}\right).
\end{aligned} \tag{3}$$

Finally equations (1) together with equations (3) form the basic elastodynamic equations which can be used to simulate elastic wave propagation in orthorhombic, HTI, VTI and isotropic medium. For HTI and VTI medium, the elastic parameters can be characterized by elastic parameters of the corresponding isotropic medium in combine with Thomsen anisotropic parameters (Thomsen 1986). In our FD modeling algorithm, we first set up indexes which can represent the anisotropy of the model before modeling and obtain the elastic parameters from isotropic elastic parameters and Thomsen anisotropic parameters in the process of modeling. In this way, we can reduce the memory cost of HTI and VTI media to the same level of isotropic media.

2.2 Numerical implementation

The standard staggered-grid FD method (Virieux 1984, 1986; Dong and McMechan 1995) is employed to solve the elastodynamic equations of velocity-stress formation. In the standard staggered-grid method, wavefield components are discretized and distributed on different numerical grids both in time and space directions in order to solve the wavefield derivatives using central difference at the corresponding grid locations. The standard staggered-grid method is especially suitable and efficient for handling orthorhombic, HTI, VTI and isotropic medium. When modeling in these media using the standard staggered-grid method, no interpolation is necessary. Thus it is computationally fast and of low memory cost compared to the rotated-staggered grid method (Saenger et al 2000) or Lebedev scheme (Lisitsa and Vishnevskiy 2010; Xu 2012). Figure 1 shows the discrete standard staggered-grid used in the FD modeling. The wavefield components and medium elastic parameters are distributed on seven different staggered grids.

The spatial and temporal derivatives of the wavefield components in elastodynamic equations (1) and (3) are calculated through

$$\frac{\partial f}{\partial x} = \frac{1}{\varDelta x} \sum_{n=1}^{L} c_n \left[f(x + n\varDelta x - 0.5\varDelta x) - f(x - n\varDelta x + 0.5\varDelta x) \right], \tag{4}$$

where c_n represents FD coefficients and L is related to the order of the FD scheme. For FD modeling, serious numerical artifacts will arise in the presence of high-frequency wavefield-components or coarse grids (Zhang and Yao 2013). Compared with reflection seismology, high dominant frequencies of the recorded signals are often observed in microseismic monitoring. For microseismic applications, amplitude fidelity and azimuthal variations of signals are critical to microseismic processing and interpretation. Thus an accurate FD scheme is required for microseismic full-waveform modeling. A FD scheme of 10th-order in space domain and 2nd-order in time domain is employed in our FWM. There are lots of optimized schemes of FD methods which try to increase modeling accuracy and reduce numerical dispersion (Holberg 1987;

Lele 1992; Liu and Sen 2009). Optimized FD coefficients are adopted in this standard staggered-grid FD modeling scheme according to Holberg (1987).

Before starting forward modeling, the space interval Δh (constant in three directions here) of the grid need to be determined by fulfilling the grid dispersion criterion $\Delta h \leq v_{min}/(2nf_m)$, where v_{min} is the minimal S-wave velocity of the model, f_m is the peak frequency of the source time function and n is the number of grid-points per wavelength. If 10th order and Holberg type of FD operators are used in the modeling, n is 3.19. For a stable numerical modeling, the time step interval Δt must satisfy the Courant-Friedrichs-Lewy criterion $\Delta t \leq \Delta h/(\sqrt{3}mv_{max})$, where v_{max} is the maximum P-wave velocity of the model and m is a factor which depends on the order and type of the FD operator. If 10th order and Holberg type of FD operators are used in the modeling, m is 1.38766.

2.3 Moment tensor source

Two kinds of wavefield excitation conditions are commonly used in full-waveform FD modeling. One is the use of body-force term which acts on equations of momentum conservation (Aboudi 1971; Kosloff et al 1989; Yomogida and Etgen 1993; Graves 1996). The other one is to add an incremental stress on stress components (Virieux 1986; Coutant et al 1995; Pitarka 1999; Narayan 2001; Li et al 2014). Compared with the direct use of body-force term, the implementation of incremental stress in FD scheme is more straightforward. In this paper, the incremental stress method is adopted in order to implement an arbitrary moment tensor source into the FWM scheme.

Seismic moment tensor can be expressed as

$$\mathbf{M} = M_0 \cdot \mathbf{m} \cdot S(t), \tag{5}$$

where M_0 is the seismic moment, $\mathbf{m}$ contains nine moment tensor components m_{ij} and $S(t)$ is the source time function. The scalar seismic moment could be expressed as $M_0 = \mu AD$, where μ is shear modulus of the rocks involved in the source area, A is the area of the rupture and D is the average displacement during rupture. The seismic moment M_0 has the same units of energy and is often used to estimate the moment magnitude scale of an earthquake. $\mathbf{m}$ is symmetric and normalized such that $\sum_{ij} m_{ij}^2 = 1$. Figure 2 shows the far-field P-wave and S-wave radiation patterns of a double-couple source, in which $m_{xx} = -m_{zz}$ and other components are 0. In figure 2, the vectors represent the polarization directions of the P- and S-waves and the color and length of the vectors represent the polarization strength.

In the staggered-grid approach, the normal stresses and shear stresses are not evaluated at the same position. Thus, applying incremental stresses directly on the stress components of the corresponding grid points will not result in an exact moment tensor source. Assuming a moment tensor point source acting at the grid position of the normal stress components, the location of the normal stress components will act as a central point. In order to obtain a symmetric moment tensor source, we evenly distribute the shear stress increments on the four adjacent shear stress grid points around the true moment tensor source location. Thus in total, there are twelve adjacent grid points around the true location of the moment tensor point source, which are numerically implemented with shear stress components (as shown by the blue grid points in figure 1). The detailed implementation of moment tensor source in staggered-grid can be found in Appendix B. In the velocity-stress FD scheme, the temporal derivative of the moment tensor is used, because the temporal derivatives of the stress components are used in the elastodynamic equations. However in the displacement-stress FD scheme, the moment tensor itself instead of its temporal derivative is adopted in the source implementation (Moczo et al 2014).

2.4 Comparisons with analytical solutions

The displacement field in a homogeneous isotropic medium can be obtained by convoluting the Green's function with the seismic moment tensor (Aki and Richards 2002, Equation 4.29)

$$\begin{aligned} u_n = M_{pq} * G_{np,q} = R_n^{ne} \frac{M_0}{4\pi\rho r^4} \int_{r/v_p}^{r/v_s} \tau S\left(t-\tau\right) d\tau + R_n^{ip} \frac{M_0}{4\pi\rho v_p^2 r^2} S\left(t - r/v_p\right) \\ + R_n^{is} \frac{M_0}{4\pi\rho v_s^2 r^2} S\left(t - r/v_s\right) + R_n^{fp} \frac{M_0}{4\pi\rho v_p^3 r} \dot{S}\left(t - r/v_p\right) + R_n^{fs} \frac{M_0}{4\pi\rho v_s^3 r} \dot{S}\left(t - r/v_s\right), \end{aligned} \tag{6}$$

where u_n is the nth component of displacement field, r is the distance between source point and receiver point, $G_{np,q}$ is the Green's function describing the wave propagation between source and receiver, R_n^{ne}, R_n^{ip}, R_n^{is}, R_n^{fp}, R_n^{fs} are near-field, intermediate-field P-wave, intermediate-field S-wave, far-field P-wave, far-field S-wave radiation pattern respectively. The comma indicates the spatial derivative with respect to the coordinate after the comma (e.g. $G_{np,q} = \partial G_{np}/\partial q$) and the dot above the source time function $S\left(t\right)$ indicates the time derivative. Thus, the displacement field in the far-field is proportional to particle velocities at the source. The elastic properties of the medium are described by density ρ, P-wave velocity v_p and S-wave velocity v_s.

The first term in equation 6 is called the near-field term, which is proportional to $r^{-4}\int_{r/v_p}^{r/v_s}\tau S(t-\tau)d\tau$ (hereafter referred to as the proportional part of near-field term). The two middle terms are called the intermediate-field terms, which are proportional to $(vr)^{-2}S(t-r/v)$. The last two terms are called the far-field terms, which are proportional to $v^{-3}r^{-1}\dot{S}(t-r/v)$. Since there is no intermediate-field region where only the intermediate-field terms dominate, so it is common to combine the intermediate-field and near-field terms. If a Ricker wavelet is used as the source time function, the integration in the near-field term is very small and its peak amplitude is approximately proportional to r/f_m (f_m is the peak frequency of the source time function and the proportional coefficient is often smaller than 10^{-6} in SI units). The derivative term of the source time function in the far-field terms is much larger than the Ricker wavelet and its integration, and its peak amplitude is approximately proportional to f_m (the proportional coefficient is approximately 6.135 for Ricker source time function).

For microseismic monitoring where high frequency data are often recorded, it is naturally favourable to consider only the far-field approximation. However, there are scenarios where the effect of near-field terms and intermediate-field terms can not be ignored (Vidalel 1995). Figure 3(a) shows the relative magnitude of peak amplitude of the proportional part of the near-field term, intermediate-field terms and far-field terms at different source-receiver distances. The elastic parameters of the medium used are $v_p = 3500\ m/s$, $v_s = 2000\ m/s$ and $\rho = 2400\ kg/m^3$. The source time function is a Ricker wavelet with a peak frequency of 40 Hz and a time delay of $1.1/f_m$ (this source time function is also used in the remaining examples). The X-axis of figure 3(a) is the ratio of the source-receiver distance to the dominant S-wave wavelength. It is obvious that at a distance larger than three or four dominant S-wave wavelengths, the far-field term dominates the wavefield (with a proportion higher than 95%). This far-field approximation is quite pervasive in microseismic monitoring because of the widely used ray-based methods and relatively high dominant frequencies of the recorded data. Furthermore most focal mechanism inversion methods are also based on the far-field approximation. However, at a distance less than two dominant S-wave wavelengths, the near-field terms and intermediate-field terms will have a non-negligible effect on the whole wavefield, and may even dominate the wavefield, especially when very close to the source region (less than one half the dominant S-wave wavelength). For microseismic downhole monitoring arrays, which are deployed close to the microseismic source area, larger errors may occur due to the significant contribution of the near-field and intermediate-field terms.

The far-field approximation is not only related to the source-receiver distance but also the radiation patterns of the near-field terms (including intermediate-terms hereafter) and far-fields terms. In directions where the strength of the far-field radiation pattern is weaker than the strength of the near-field radiation pattern, the contribution of near-field terms may bias the far-field approximation in the "far" field. Figure 3(b) is a 3D map which shows the far-field distance of a double-couple source in different directions. The elastic property of the medium is the same as before with the moment tensor source radiation pattern displayed in figure 2. The far-field distance is expressed in terms of S-wave wavelength. The color and shape in the figure shows the distance where the far-field terms will occupy 80% energy in the whole wavefield. Beyond this distance, we can consider that the far-field terms dominate the wavefield.

Figure 3(b) reveals an obvious directional feature. If there were no difference in radiation pattern between the far-field and near-field terms, figure 3(b) would show an uniform spherical distribution in different directions. However the difference in radiation patterns has distorted the scope where the near-field could exert influence on the wavefield. In directions where the near-field radiation pattern is strong and the far-field radiation is weak, the distance in which the near-field terms have a non-negligible influence on the whole wavefield has been extended. The far-field distance in different directions in figure 3(b) ranges from about 2 times the dominant S-wave wavelength to 12 times the dominant S-wave wavelength. Thus, great care must be taken when receivers have been deployed in these directions. Figure 3(c) shows the variation of relative magnitude in two specific directions for the same double-couple source. The radiation patterns of the near-, intermediate- and far-field terms have been taken into consideration. When considering source radiation pattern, the far-field distance shows strong dependence on directions. The far-field distance has been extended to 12 times the dominant S-wave wavelength in direction of 5° zenith angle and 0° azimuth angle (shown as the dashed lines). The far-field terms need a farther distance to dominate in the whole wavefield. In this way, we can find out the acceptable distance in different directions where the far-field approximation is acceptable for different types of source. This will be very helpful for array deployment and data interpretation in microseismic monitoring.

Full waveform FD modeling can provide a step improvement in accurately modeling all kinds of wave phenomena both in the near-field and far-field. Figure 4(a) compares the synthetic displacement field in the Y direction for finite-difference solution and the analytical result under the same medium parameter settings. For generality, a non-double-couple moment tensor source is adopted in the simulation. The non-double-couple moment tensor is given by

$$\mathbf{m} = \begin{pmatrix} 0.4532 & 0.2789 & 0.1743 \\ 0.2789 & -0.5926 & 0.1046 \\ 0.1743 & 0.1046 & 0.4532 \end{pmatrix}. \tag{7}$$

For the finite-difference simulation, the spatial interval and time interval are 5 m and 0.1 ms respectively. The source-receiver distances of the twelve receivers range from $0.5\lambda_s$ to $8\lambda_s$ to account for both near-field and far-field scenarios (λ_s is the dominant S-wave wavelength, which is 50 m in this simulation experiment). The twelve receivers are also deployed in different directions. As shown in figure 4(a), the waveform fidelity of the finite-difference results is in good agreement for both the near-field and far-field terms, with no obvious amplitude differences or phase shifts with respect to the analytical solution. This is also verified by figure 4(b) which shows the relative error of the peak amplitude with respect to the analytical solution. The relative errors of the finite-difference modeling are within 1% both in the near-field and far-field. However the relative errors of far-field approximation are much larger than that of the finite-difference method especially in the near-field. Considering the inevitable simulation error brought in by numerical discretization, the accuracy of this finite-difference simulation is adequate. The accuracy of the finite-difference method can be further improved by applying very fine simulation grid and adopting smaller time step. Thus, the finite-difference modeling can provide full-waveform information and more accurate results than far-field approximation.

3 Modeling examples

3.1 Anisotropic Layered Model

The subsurface medium can range in complexity, both in terms of elastic heterogeneity and anisotropy. In order to inspect the influence of anisotropy on the wavefield from a microseismic event, a simple block velocity model with three layers is examined. As shown in figure 5 (a), a microseismic event is located in the middle of the model. Both a surface array and a vertical downhole array are deployed to record the microseismic data. The surface array has 90000 geophones deployed uniformly along the free surface at 10 m intervals. The vertical downhole array is located at a horizontal distance of 283 m and an azimuth of 135° relative to the microseismic source (i.e. the middle of the model). The downhole array has 500 geophones with intervals of 5 m. In the second layer, where the microseismic event is located, we examine three submodels having three different types of anisotropy. In the first submodel, no anisotropy is introduced, which implies an isotropic layered setting. In the second submodel, the second layer is set to be VTI, which is used to simulate shale having horizontal stratification. In the third submodel, the second layer is set to be HTI, which is used to simulate rock with vertical fractures. For all the submodels, a vertical strike-slip event is used to simulate the microseismic source, which means only m_{xy} and m_{yx} are non-zero in the seismic moment tensor. The elastic parameters of the isotropic layered model are shown in table 2. The VTI medium in the second example has Thomsen parameters of $\varepsilon = 0.334$, $\gamma = 0.575$, $\delta = 0.73$, which is a measured anisotropy in clayshale (Thomsen 1986). The HTI medium in the third submodel is constructed by rotating the VTI medium of the second submodel anticlockwise along the Y-axis by 90°.

The P- and S-wave velocity anisotropy of the VTI and HTI media used in the second layer in the submodels are shown in figure 5 (c-e) and figure 5 (f-h), respectively (Walker and Wookey 2012). The relative variation for the P-, fast and slow S-wave velocity in the VTI medium are 29.2%, 46.6% and 28.4% respectively. The velocity anisotropy of the HTI medium can be easily obtained by rotation.

Figure 6 (a-c) shows horizontal wavefield slices of particle velocity in the Y direction for the three submodels, where the wavefield is recorded at the depth of microseismic source. Different types of waves can be identified in these wavefield slices. For figure 6(a), the isotropic case, only the P- and S-wave are identified in the wavefield slice. In the VTI anisotropic example shown in figure 6(b), S-wave splitting is clearly observed seen by the distinct fast S-wave (qS1-wave) and slow S-wave (qS2-wave) in the wavefield. As the second layer is transversely isotropic, the wavefront in the horizontal slice does not show anisotropic velocity variation in the different propagation directions. In the third example, where the second layer is HTI medium, a more complex wavefield is observed. Due to strong anisotropy, the wavefronts of the different types of waves show strong anisotropy in the different propagation directions, and where wavefront triplication is also observed in the slice.

Figure 6 (d-f) shows vertical wavefield slices of the particle velocity in the Y direction for the three submodels, where the vertical slice bisects the same Y-position of the microseismic source. Due to the existence of layer boundaries in these vertical slices, reflected waves, transmitted waves and mode-converted waves (e.g., converted

PS-waves and converted SP-waves) appear in the wavefield slices, thus making the wavefield more complicated. For the VTI submodel, the vertical wavefield slice is not located in the transversely isotropic plane, thus strong anisotropy can be observed in the shape of the wavefront (as shown in figure 6(e)). For the HTI submodel, where the orientation of the HTI medium is oriented such that the transversely isotropic plane is parallel to the Y-axis, the vertical wavefield displays strong anisotropy in the wavefront (as shown in figure 6(f)). The presence of seismic anisotropy has made the wavefield much more complex compared to the isotropic case, increasing the complexity of microseismic processing, such as event detection and travel-time picking.

Downhole array

The recorded seismograms for the downhole array are shown in figure 7. The recorded seismograms are the particle velocity component in the Y direction. The direct P- and S-wave are automatically picked in the recorded wavefields. Compared with the seismograms in the isotropic case, the seismograms for the anisotropic submodels are much more complicated. Due to S-wave splitting, more mode-converted and multi-reflected waves appear in the recorded data, thus making microseismic event detection and arrival-time picking more difficult. When many microseismic events are triggered in the target area within a short time, the extra complexity and aliasing in wavefield introduced by the medium anisotropy of the target area will make microseismic location difficult.

To further study the influence of anisotropy on microseismic monitoring, travel-times and peak amplitudes of the direct P-wave in the three submodels are extracted and compared. As figure 8 shows, when the subsurface medium shows strong anisotropy, the amplitudes and travel-times of the direct P-wave will be variable. The maximum relative differences in travel-time and peak amplitude are 16% and 86% for the VTI case, and 18% and 50% for the HTI case. The travel-time and amplitude differences between the anisotropic models and the isotropic model are not constant, and vary with wave propagation direction due to anisotropy. The amplitude of the recorded waveforms is mainly affected by the radiation pattern of the source, coupling between different phases and the elastic properties of the media such as impedance and attenuation. Because of seismic anisotropy, wave velocity varies with different propagation directions. Thus the ray path and media elastic parameters in anisotropic cases are different with those in isotropic case. In this way, the seismic anisotropy has affected the travel-time and amplitude of the recorded waves and hence the observed radiation pattern of the microseismic source. Thus without considering seismic anisotropy, the variation in travel-time and amplitude in the different directions will bias the final result, thus contributing to large errors in inverted source location and mechanism. As shown in figure 8(b), when geophones are located in the anisotropic layer, the travel-time difference of the direct P-wave in the VTI and HTI models with respect to the isotropic model exhibit opposing trends. For the VTI model, the travel-time difference increases with the take-off angle of the seismic rays, whereas for the HTI model, the travel-time difference decreases with the take-off angle of the seismic rays. The travel-time difference can be expressed by

$$\Delta t = \frac{l_{ref}}{v_{ref}} - \frac{l_{ani}}{v_{ani}}, \tag{8}$$

where l represents the ray path in the isotropic reference medium or anisotropic medium; v_{ref} is the average group velocity along the ray path in the reference medium (which is the P-wave velocity of the isotropic model here); v_{ani} is the average group velocity along the ray path in the anisotropic medium. The average group velocity of the reference medium v_{ref} will only affect the sign of the travel-time difference and not the trend of the travel-time difference. In practice, the reference velocity can be determined by well logging data, which is a approximation for the velocity in the vertical direction. For simplicity, the ray path in the isotropic and anisotropic media could be considered approximately the same, which is often the case in the near-field and for smooth velocity models. Thus the travel-time difference is proportional to the length of ray path and average group velocity of the anisotropic medium along the ray path. Under the current modeling geometry, the length of the ray path decreases with the take-off angle of the seismic rays. However, the downhole array is deployed near the source region and thus velocity variation of the anisotropic medium along different propagation directions is the main control factor for travel-time differences. When the recording array is deployed far enough away from the source region, such as surface arrays, the length of the ray path should be taken into consideration when analysing travel-time differences.

As we have shown, the different types of velocity anisotropy can cause different trends in travel-time differences. Figure 9 shows the velocity surfaces in the profile of the downhole array for the isotropic model, VTI model and HTI model. The P-wave velocity towards the directions of downhole geophones in the second layer are calculated and shown in figure 10(b). For the VTI medium, the P-wave velocity increases with the take-off angle. However, for the HTI medium, the P-wave velocity decreases with the take-off angle at this particular azimuth. The normalized travel-time difference of the direct P-wave for the downhole geophones in the second layer is shown in figure 10(c). In figure 10(c), the effect of the ray path has been considered and eliminated, thus the travel-time differences are only influenced by the P-wave velocity. Figure 10(b) and figure 10(c) show strong similarity and potentially provides a way to estimate the anisotropy of the target zone in microseismic monitoring. As well, the VTI and HTI media can be distinguished using a downhole array.

The variation in travel-times and peak-amplitudes for the fast S-wave (S-wave in isotropic case) in the different models are shown in figure 11. In figure 11(c), the peak amplitudes of the fast S-wave in the VTI model shows a big difference with that in the isotropic and HTI models. From the recorded waveform in figure 12 (a-b), we can clearly see that seismic anisotropy has completely changed the radiation pattern of the S-wave in the VTI model.

The velocity difference or travel-time difference between the fast S-wave and the slow S-wave can be used to describe the shear-wave anisotropy in an anisotropic medium. Large velocity differences between fast and slow shear-waves will contribute to strong shear-wave splitting (i.e. splitting time). Figure 12 (c-d) shows the variation of shear-wave anisotropy in the VTI and HTI models. The travel-time difference between the fast S-wave and the slow S-wave are also extracted and displayed in figure 13(a). The normalized travel-time difference after eliminating the influence of the ray-path (figure 13(b)) shows good consistency with the velocity difference (figure 13(c)) suggesting that this is a feasible way to estimate the anisotropy of the subsurface in microseismic monitoring.

Surface array

Figure 14 shows seismic profiles recorded by the surface array. The direct P-wave arrivals are automatically picked in the recorded wavefields. Four traces in figure 14 are extracted and shown in figure 15. Due to the strong seismic anisotropy, the received seismic waveforms for the VTI and HTI submodels are quite different compared to the isotropic case. More phases can be observed in the anisotropic models because of shear-wave splitting. If care is not taken, these phases could be identified as true microseismic events having detrimental effect on microseismic interpretation.

Figure 16 shows the travel-times of the direct P-wave along the free surface. As the surface array is deployed uniformly on the free surface and the microseismic source is located just below the middle of the surface array, the travel-times of the seismic waves in the isotropic layered media should be symmetrical about the epicenter, as can be seen in figure 16(a), where the travel-times of the direct P-wave are circular. In the VTI model, the transverse isotropic symmetry plane is in the horizontal plane, and so the travel-times of the direct P-wave are also circular (figure 16(b)). The magnitude of travel-time differs from the isotropic case due to the presence of anisotropy. However, in HTI model, the transverse isotropic symmetry plane is vertical, thus velocity anisotropy in the horizontal plane will contribute to an asymmetric distribution about the epicenter. As figure 16(c) shows, travel-times of the direct P-wave are ellipses in the HTI model. The major axis of ellipse is parallel to the isotropic plane of the HTI medium, which is along the orientation of the fracture planes. The ratio of the major and minor axes of the ellipse is proportional to the strength of anisotropy. Travel-time differences of the direct P-wave between the anisotropic models and the isotropic model are shown in figure 17, which clearly exhibits the different characteristics of VTI and HTI media and the alteration of travel-times introduced by seismic anisotropy.

Figure 18 shows the peak amplitudes and also the polarization of the direct P-wave. The maximum relative difference of peak amplitude can be as large as 50% for VTI and HTI, which means seismic anisotropy can have a large influence on source mechanism characterization, such as moment tensor inversion. As shown in figure 18, the peak amplitudes of the direct P-wave in anisotropic case is smaller than that in isotropic case. This will cause an underestimate of the seismic moment M_0 in the presence of anisotropy when only direct P-waves are used in the source magnitude estimation. In figure 18, the polarizations of the direct P-wave have not been significantly affected by seismic anisotropy. The peak amplitude differences of the direct P-wave between the anisotropic models and the isotropic model are also shown in figure 19, which clearly shows the alteration of amplitudes introduced by seismic anisotropy.

3.2 Anisotropic Overthrust Model

Based on the previous simple models, it is not surprising that microseismic imaging in complex media is a challenge. In complex media, the influence of seismic anisotropy could be further distorted due to the presence of elastic heterogeneity. In order to study the influence of seismic anisotropy on microseismic monitoring in complex media, we apply full waveform modeling in the 3D isotropic and anisotropic SEG/EAGE overthrust model (Aminzadeh et al 1997). Three overthrust models with different types of anisotropy are used in the simulations. The P-wave velocity of the overthrust model is shown in figure 20. The overthrust model has a size of $801 * 801 * 187$ in X, Y and Z directions. The same double-couple source (vertical strike-slip) is placed in the middle of the 3D model, (i.e., grid coordinate 400, 400 and 93 in X, Y and Z directions). Around the source, an anisotropic region is set up (marked by the black lines in figure 21). In the anisotropic region, different models are set to have different types of anisotropy, which are isotropy, VTI anisotropy and HTI anisotropy. The VTI anisotropy has the same Thomsen anisotropic parameters (i.e., $\varepsilon = 0.334$, $\gamma = 0.575$ and $\delta = 0.73$) as the former VTI modeling example. The HTI media is constructed by rotating the VTI media counter-clockwise along Y-axis by 90°. Figure 21 shows three profiles of the overthrust model, in which the source location and anisotropic volume are clearly marked. As figure 21 shows, the 3D SEG/EAGE overthrust model contains lots of faults (figure 21(b) and 21(c)) and fluvial deposits (figure 21(a)), which are suitable for studying the influence of anisotropy in complex heterogeneous media. Both a surface array ($149 * 149$ geophones at 25 m intervals) and a vertical downhole array (127 geophones at 5 m intervals) are used to record the microseismic data in the simulations.

Figure 22 shows the wavefield snapshots of these three modelings. Compared with wavefields in isotropic model, the wavefields in anisotropic model is much more complex due to seismic anisotropy, especially in the anisotropic region. These complexity raises from the shear-wave splitting and velocity contrast between isotropic region and anisotropic region.

Figure 23 shows the recorded seismograms of the downhole array in different models. The strong heterogeneity has made the wavefields very complex, where abundant reflected and multiples can be seen in the recorded seismograms. In the presence of anisotropy, the heterogeneity has added to the general complexity of an isotropic phenomena. Significant differences of the recorded seismograms between the anisotropic models and the isotropic model can be seen in figure 23.

The travel-times and peak amplitudes of the direct P-wave have been automatically picked and displayed in figure 24. As with the previous analysis in the layered model, the travel-time differences of the direct P-wave in the VTI model increases with take-off angle of the rays and exhibits an upside down U shape pattern in the downhole array. On the contrary, the travel-time differences of the direct P-wave in the HTI model exhibits an opposite trend in the downhole array. The amplitudes of the direct P-waves are also different in the anisotropic scenarios. The maximum relative differences for travel-times and amplitudes are 17% and 80% respectively in the anisotropic models.

The seismic profiles recorded by surface array are shown in figure 25. Significant differences in the recorded wavefields can be observed between the isotropic, VTI and HTI models. The direct P-waves recorded by the surface array are automatically picked. The picked travel-times and peak amplitudes of the direct P-wave are shown in figures 26 and 27. Because of the complexity of the recorded wavefields and weak strength of the direct P-wave, the automatic picking is not perfect. Some picking errors can be seen in the figures and the picked peak amplitudes are blurred. However the radiation pattern of the direct P-wave can be recognised both in the isotropic and the VTI models. The radiation pattern of the direct P-wave in HTI model is affected by picking error and cannot be recognised easily. In this situation, the manual picking is required. The surface array is symmetrical about the epicenter of the source. The travel-times of the direct P-wave in VTI model maintain the circular distribution as in the isotropic model because the transverse isotropic symmetry plane is in the horizontal plane. However the travel-times of the direct P-wave in HTI model exhibit an ellipse distribution because of the anisotropy in the horizontal plane. The major axis of the ellipse is parallel to the direction of the isotropic plane of the HTI media, and the minor axis of the ellipse is parallel to the direction of the symmetry axis of the HTI media. And the ratio of the major axis to the minor axis is proportional to the strength of anisotropy. In reality, if a microseismic source is located, we can pick out the same phases with the same offset but at different azimuth angles in the surface array and compare the travel-time of these phases. As the FracStar array is increasingly used in the surface microseismic monitoring, it is not hard to find receivers which have the same offset but different azimuth angles. Thus in this way, we can estimated the orientation and density of the fractures using surface array in microseismic monitoring when the seismic anisotropy is caused by the vertical cracks induced by hydraulic fracturing. Through analysing anisotropy using surface array data of different events during hydraulic fracturing, we can also evaluate the fracturing effect and gain more knowledge about the fracturing process. Even through the ray path in different azimuth is different due to horizontal heterogeneity, the travel-time is not affect too much by the ray path. The influence of seismic anisotropy in travel-times is still observable and is more significant at relatively large offsets. This demonstrate it is feasible to estimate the seismic anisotropy of the complex subsurface media using surface array. The polarization of the direct P-wave is not seriously affected by anisotropy. However the variation in amplitude caused by anisotropy could introduce biases in moment tensor inversion.

4 Discussions and Conclusion

The primary focus of this study was to develop an efficient FD forward modeling tool with arbitrary moment tensor source, which can be used for simulating wave propagation phenomena in anisotropic media for microseismic monitoring. We have shown how to implement an symmetrical moment tensor source into the staggered-grid FD modeling scheme. We simulated and analysed the wavefields in both a 3D layered and a 3D overthrust anisotropic model. Because both VTI and HTI anisotropy are common in shale or fractured media, we focused only on wavefields in VTI and HTI media.

In the complex overthrust model, when analysing travel-time differences, we did not eliminate the influence of ray path differences as we did in the layered model. However, the variation trends of travel-time differences with respect to take-off angle in VTI and HTI anisotropic scenarios are still established in the downhole array. And the variation of travel-time in the surface array also exhibit the same phenomenon as with in layered model. This is because the anisotropy is strong enough that the influence of velocity variation surmounts that of ray path differences in travel-time.

However, when the variation of ray path is significant or the anisotropy is weak, the influence of ray path must be considered and eliminated in order to correctly evaluate the anisotropy. This will involve ray tracing in heterogeneous and/or anisotropic media.

Seismic anisotropy is an important property of shale rocks, where most hydraulic fracturing is implemented. The fracture networks induced by hydraulic fracturing are also responsible for seismic anisotropy in the subsurface. We have shown that seismic anisotropy can have a significant influence on travel-time and amplitude of the recorded seismic waves, thus contributing to larger deviations in source location and moment tensor inversion in microseismic monitoring. These variations in travel-time and amplitude caused by seismic anisotropy can also be used to evaluated the anisotropy of the subsurface, especially for estimating the strength of anisotropy in HTI media using surface array. In vertical downhole array, the travel-time differences of direct P-waves will normally increase with the take-off angle of the seismic rays in VTI media, while the travel-time differences of direct P-waves will normally decrease with the take-off angle of the seismic rays in HTI media. In surface array, the travel-times of direct P-wave exhibit a circular distribution in isotropic and VTI media, while the travel-times of direct P-wave exhibit an ellipse distribution in HTI media. The strength of seismic anisotropy can be estimated by calculating the ratio of the major axis of the ellipse to the minor axis of the ellipse. The direction of the symmetry axis of the HTI media (i.e., the orientation of fracture planes) can also be estimated through identifying the direction of the major axis of the ellipse. The fracturing effect can also be evaluated through anisotropy analysis of different events in hydraulic fracturing. Although the polarization of direct waves is less affected by anisotropy, the deviation in source location will be accumulated into the source mechanism determination and make source mechanism determination problematic. Since we have focused on full waveform modeling in heterogeneous and anisotropic media in this paper, a quantitative analysis of the influence of anisotropy on microseismic source location is not robustly studied.

Compared with surface array, downhole array is more vulnerable to seismic anisotropy. Thus extra care should be taken when conducting microseismic monitoring in anisotropic media using downhole array. Analysing seismic anisotropy of the recorded microseismic data provides a feasible way to evaluate the fracture networks induced by hydraulic fracturing, and can also improve the accuracy of microseismic source location and mechanism characterization.

Acknowledgements We wish to thank Institute of Applied Geoscience and Institute of Geophysics and Tectonics, University of Leeds for supporting this work. The work of P. Shi was supported by a China Scholarship Council/University of Leeds scholarship.

Appendix A Moment tensor source radiation pattern

A seismic moment tensor is the combination of nine generalized couple forces which have three possible directions and act on three possible arms. It can be used to simulate seismic sources which have body-force equivalent given by pairs of forces. The seismic moment tensor source equivalent has been verified by the radiation patterns of teleseismic data and also seismic data obtained very close to the source region (Aki and Richards 2002). A common seismic moment tensor can be expressed as

$$\mathbf{m} = \begin{pmatrix} m_{xx} & m_{xy} & m_{xz} \\ m_{yx} & m_{yy} & m_{yz} \\ m_{zx} & m_{zy} & m_{zz} \end{pmatrix}. \tag{9}$$

The source radiation pattern of P- and S-waves can be derived from the Green's function in an isotropic elastic medium (Aki and Richards 2002). For far-field P-waves, the radiation pattern is given by

$$R_n^p = \gamma_n \gamma_p \gamma_q m_{pq}. \tag{10}$$

For far-field S-waves, the radiation pattern is given by

$$R_n^s = -(\gamma_n \gamma_p - \delta_{np}) \gamma_q m_{pq}. \tag{11}$$

In these equations, R_n represents the nth component of the radiation pattern vector for P- or S-wave, γ_p is the direction cosine of the source-receiver unit direction vector, m_{pq} is the moment tensor component. Implicit summation over the repeated index is applied in these equations.

If using the unit basis vectors in spherical coordinates, then we can further obtain the radiation pattern for P-waves (Chapman 2004)

$$\begin{aligned} R^p = &\left(m_{xx}\cos^2\phi + m_{yy}\sin^2\phi + m_{xy}\sin 2\phi\right)\sin^2\theta \\ &+ m_{zz}\cos^2\theta + \left(m_{zx}\cos\phi + m_{yz}\sin\phi\right)\sin 2\theta, \end{aligned} \tag{12}$$

for SV-waves

$$\begin{aligned} R^{sv} = &\frac{1}{2}\left(m_{xx}\cos^2\phi + m_{yy}\sin^2\phi - m_{zz} + m_{xy}\sin 2\phi\right)\sin 2\theta \\ &+ \left(m_{zx}\cos\phi + m_{yz}\sin\phi\right)\cos 2\theta, \end{aligned} \tag{13}$$

for SH-waves

$$R^{sh} = \left(\frac{1}{2}\left(m_{yy} - m_{xx}\right)\sin 2\phi + m_{xy}\cos 2\phi\right)\sin\theta + \left(m_{yz}\cos\phi - m_{zx}\sin\phi\right)\cos\theta, \quad (14)$$

in which θ and ϕ represent the coordinate components (polar angle and azimuth angle) in the spherical coordinates respectively.

Appendix B Moment tensor source implementation in staggered-grid

The complete formulation for a moment tensor point source acting at the staggered-grid node i,j,k (i.e. the grid position of the normal stress components) is given by

$$\begin{aligned}
\tau_{xx}(i,j,k) &= \tau_{xx}(i,j,k) - \frac{\Delta t}{V}\frac{\partial M_{xx}(t)}{\partial t},\\
\tau_{yy}(i,j,k) &= \tau_{yy}(i,j,k) - \frac{\Delta t}{V}\frac{\partial M_{yy}(t)}{\partial t},\\
\tau_{zz}(i,j,k) &= \tau_{zz}(i,j,k) - \frac{\Delta t}{V}\frac{\partial M_{zz}(t)}{\partial t},\\
\tau_{yz}(i,j+1/2,k+1/2) &= \tau_{yz}(i,j+1/2,k+1/2) - \frac{\Delta t}{4V}\frac{\partial M_{yz}(t)}{\partial t},\\
\tau_{yz}(i,j+1/2,k-1/2) &= \tau_{yz}(i,j+1/2,k-1/2) - \frac{\Delta t}{4V}\frac{\partial M_{yz}(t)}{\partial t},\\
\tau_{yz}(i,j-1/2,k+1/2) &= \tau_{yz}(i,j-1/2,k+1/2) - \frac{\Delta t}{4V}\frac{\partial M_{yz}(t)}{\partial t},\\
\tau_{yz}(i,j-1/2,k-1/2) &= \tau_{yz}(i,j-1/2,k-1/2) - \frac{\Delta t}{4V}\frac{\partial M_{yz}(t)}{\partial t},\\
\tau_{xz}(i+1/2,j,k+1/2) &= \tau_{xz}(i+1/2,j,k+1/2) - \frac{\Delta t}{4V}\frac{\partial M_{xz}(t)}{\partial t},\\
\tau_{xz}(i+1/2,j,k-1/2) &= \tau_{xz}(i+1/2,j,k-1/2) - \frac{\Delta t}{4V}\frac{\partial M_{xz}(t)}{\partial t},\\
\tau_{xz}(i-1/2,j,k+1/2) &= \tau_{xz}(i-1/2,j,k+1/2) - \frac{\Delta t}{4V}\frac{\partial M_{xz}(t)}{\partial t},\\
\tau_{xz}(i-1/2,j,k-1/2) &= \tau_{xz}(i-1/2,j,k-1/2) - \frac{\Delta t}{4V}\frac{\partial M_{xz}(t)}{\partial t},\\
\tau_{xy}(i+1/2,j+1/2,k) &= \tau_{xy}(i+1/2,j+1/2,k) - \frac{\Delta t}{4V}\frac{\partial M_{xy}(t)}{\partial t},\\
\tau_{xy}(i+1/2,j-1/2,k) &= \tau_{xy}(i+1/2,j-1/2,k) - \frac{\Delta t}{4V}\frac{\partial M_{xy}(t)}{\partial t},\\
\tau_{xy}(i-1/2,j+1/2,k) &= \tau_{xy}(i-1/2,j+1/2,k) - \frac{\Delta t}{4V}\frac{\partial M_{xy}(t)}{\partial t},\\
\tau_{xy}(i-1/2,j-1/2,k) &= \tau_{xy}(i-1/2,j-1/2,k) - \frac{\Delta t}{4V}\frac{\partial M_{xy}(t)}{\partial t},
\end{aligned} \quad (15)$$

where $V = \Delta x \cdot \Delta y \cdot \Delta z$ is the effective volume of the grid cell, Δt is the time spacing of FD modeling. This is the formulation of source terms in the velocity-stress FD scheme. For moment tensor source implementation in the displacement-stress FD scheme, the moment tensor itself is used instead of its temporal derivative. And the time spacing item in these equations also disappears.

References

Aboudi J (1971) Numerical simulation of seismic sources. Geophysics 36(5):810–821

Aki K, Richards PG (2002) Quantitative seismology, vol 1. University Science Books

Al-Harrasi O, Al-Anboori A, Wüstefeld A, Kendall JM (2011) Seismic anisotropy in a hydrocarbon field estimated from microseismic data. Geophys Prospect 59(2):227–243

Aminzadeh F, Jean B, Kunz T (1997) 3-D salt and overthrust models. Society of Exploration Geophysicists

Angus D, Aljaafari A, Usher P, Verdon J (2014) Seismic waveforms and velocity model heterogeneity: Towards a full-waveform microseismic location algorithm. J Appl Geophys 111:228–233

Artman B, Podladtchikov I, Witten B (2010) Source location using time-reverse imaging. Geophys Prospect 58(5):861–873

Baysal E, Kosloff DD, Sherwood JW (1983) Reverse time migration. Geophysics 48(11):1514–1524

Boyd OS (2006) An efficient matlab script to calculate heterogeneous anisotropically elastic wave propagation in three dimensions. Comput Geosci 32(2):259–264

Brzak K, Gu YJ, Ökeler A, Steckler M, Lerner-Lam A (2009) Migration imaging and forward modeling of microseismic noise sources near southern Italy. Geochem Geophys Geosyst 10(1)

Chambers K, Dando BD, Jones GA, Velasco R, Wilson SA (2014) Moment tensor migration imaging. Geophys Prospect 62(4):879–896

Chapman C (2004) Fundamentals of seismic wave propagation. Cambridge university press

Coutant O, Virieux J, Zollo A (1995) Numerical source implementation in a 2d finite difference scheme for wave propagation. Bull Seismol Soc Am 85(5):1507–1512

Dong Z, McMechan GA (1995) 3-d viscoelastic anisotropic modeling of data from a multicomponent, multiazimuth seismic experiment in northeast texas. Geophysics 60(4):1128–1138

Gajewski D, Tessmer E (2005) Reverse modelling for seismic event characterization. Geophys J Int 163(1):276–284

Graves RW (1996) Simulating seismic wave propagation in 3d elastic media using staggered-grid finite differences. Bull Seismol Soc Am 86(4):1091–1106

Grechka V, Yaskevich S (2013a) Azimuthal anisotropy in microseismic monitoring: A bakken case study. Geophysics 79(1):KS1–KS12

Grechka V, Yaskevich S (2013b) Inversion of microseismic data for triclinic velocity models. Geophys Prospect 61(6):1159–1170

Grechka V, Singh P, Das I (2011) Estimation of effective anisotropy simultaneously with locations of microseismic events. Geophysics 76(6):WC143–WC155

Hobro J, Williams M, Calvez JL (2016) The finite-difference method in microseismic modeling: Fundamentals, implementation, and applications. The Leading Edge 35(4):362–366

Holberg O (1987) Computational aspects of the choice of operator and sampling interval for numerical differentiation in large-scale simulation of wave phenomena. Geophys Prospect 35(6):629–655

Jin S, Jiang F, Zhu X (2013) Viscoelastic modeling with simultaneous microseismic sources. In: SEG Technical Program Expanded Abstracts 2013, Society of Exploration Geophysicists, pp 3355–3359

Johnston JE, Christensen NI (1995) Seismic anisotropy of shales. J Geophys Res 100(B4):5991–6003

Kawakatsu H, Montagner JP (2008) Time-reversal seismic-source imaging and moment-tensor inversion. Geophys J Int 175(2):686–688

Kelly K, Ward R, Treitel S, Alford R (1976) Synthetic seismograms: A finite-difference approach. Geophysics 41(1):2–27

Kosloff D, Queiroz Filho A, Tessmer E, Behle A (1989) Numerical solution of the acoustic and elastic wave equations by a new rapid expansion method. Geophys Prospect 37(4):383–394

Lele SK (1992) Compact finite difference schemes with spectral-like resolution. J Comput Phys 103(1):16–42

Li D, Helmberger D, Clayton RW, Sun D (2014) Global synthetic seismograms using a 2-d finite-difference method. Geophys J Int 197(2):1166–1183

Li H, Wang R, Cao S (2015) Microseismic forward modeling based on different focal mechanisms used by the seismic moment tensor and elastic wave equation. J Geophys Eng 12(2):155

Li J, Sadi Kuleli H, Zhang H, Nafi Toksöz M (2011) Focal mechanism determination of induced microearthquakes in an oil field using full waveforms from shallow and deep seismic networks. Geophysics 76(6):WC87–WC101

Linzer L, Mhamdi L, Schumacher T (2015) Application of a moment tensor inversion code developed for mining-induced seismicity to fracture monitoring of civil engineering materials. J Appl Geophys 112:256–267

Lisitsa V, Vishnevskiy D (2010) Lebedev scheme for the numerical simulation of wave propagation in 3d anisotropic elasticity‡. Geophys Prospect 58(4):619–635

Liu Y, Sen MK (2009) An implicit staggered-grid finite-difference method for seismic modelling. Geophys J Int 179(1):459–474

Moczo P, Kristek J, Gális M (2014) The finite-difference modelling of earthquake motions: Waves and ruptures. Cambridge University Press

Nakata N, Beroza GC (2016) Reverse time migration for microseismic sources using the geometric mean as an imaging condition. Geophysics 81(2):KS51–KS60

Narayan J (2001) Site-specific strong ground motion prediction using 2.5-d modelling. Geophys J Int 146(2):269–281

O'Brien G, Lokmer I, De Barros L, Bean CJ, Saccorotti G, Metaxian JP, Patané D (2011) Time reverse location of seismic long-period events recorded on mt etna. Geophys J Int 184(1):452–462

Pitarka A (1999) 3d elastic finite-difference modeling of seismic motion using staggered grids with nonuniform spacing. Bull Seismol Soc Am 89(1):54–68

Rössler D, Rümpker G, Krüger F (2004) Ambiguous moment tensors and radiation patterns in anisotropic media with applications to the modeling of earthquake mechanisms in w-bohemia. Stud Geophys Geod 48(1):233–250

Rüger A (1997) P-wave reflection coefficients for transversely isotropic models with vertical and horizontal axis of symmetry. Geophysics 62(3):713–722

Saenger EH, Gold N, Shapiro SA (2000) Modeling the propagation of elastic waves using a modified finite-difference grid. Wave Motion 31(1):77–92

Saenger EH, Kocur GK, Jud R, Torrilhon M (2011) Application of time reverse modeling on ultrasonic non-destructive testing of concrete. Appl Math Model 35(2):807–816

Sayers CM (1998) Misalignment of the orientation of fractures and the principal axes for p and s waves in rocks containing multiple non-orthogonal fracture sets. Geophys J Int 133(2):459–466

Schoenberg M, Sayers CM (1995) Seismic anisotropy of fractured rock. Geophysics 60(1):204–211

Sheriff RE, Geldart LP (1995) Exploration seismology. Cambridge university press

Šílenỳ J, Hill DP, Eisner L, Cornet FH (2009) Non–double-couple mechanisms of microearthquakes induced by hydraulic fracturing. J Geophys Res 114(B8)

Song F, Toksöz MN (2011) Full-waveform based complete moment tensor inversion and source parameter estimation from downhole microseismic data for hydrofracture monitoring. Geophysics 76(6):WC103–WC116

Steiner B, Saenger EH, Schmalholz SM (2008) Time reverse modeling of low-frequency microtremors: Application to hydrocarbon reservoir localization. Geophys Res Lett 35(3)

Stierle E, Vavryčuk V, Kwiatek G, Charalampidou EM, Bohnhoff M (2016) Seismic moment tensors of acoustic emissions recorded during laboratory rock deformation experiments: sensitivity to attenuation and anisotropy. Geophys J Int 205(1):38–50

Teanby N, Kendall JM, Jones R, Barkved O (2004) Stress-induced temporal variations in seismic anisotropy observed in microseismic data. Geophys J Int 156(3):459–466

Thomsen L (1986) Weak elastic anisotropy. Geophysics 51(10):1954–1966

Tromp J, Komattisch D, Liu Q (2008) Spectral-element and adjoint methods in seismology. Commun Comput Phys 3(1):1–32

Tsvankin I (1997) Anisotropic parameters and p-wave velocity for orthorhombic media. Geophysics 62(4):1292–1309

Usher P, Angus D, Verdon J (2013) Influence of a velocity model and source frequency on microseismic waveforms: some implications for microseismic locations. Geophys Prospect 61(s1):334–345

Vavryčuk V (2005) Focal mechanisms in anisotropic media. Geophys J Int 161(2):334–346

Vavryčuk V (2007) On the retrieval of moment tensors from borehole data. Geophys Prospect 55(3):381–391

Verdon J, Kendall JM, Wüstefeld A (2009) Imaging fractures and sedimentary fabrics using shear wave splitting measurements made on passive seismic data. Geophys

J Int 179(2):1245–1254

Vernik L, Liu X (1997) Velocity anisotropy in shales: A petrophysical study. Geophysics 62(2):521–532

Vidalel JE (1995) Near-field deformation seen on distant broadband. Geophys Res Lett 22(1):1–4

Virieux J (1984) Sh-wave propagation in heterogeneous media: Velocity-stress finite-difference method. Geophysics 49(11):1933–1942

Virieux J (1986) P-sv wave propagation in heterogeneous media: Velocity-stress finite-difference method. Geophysics 51(4):889–901

Virieux J, Operto S (2009) An overview of full-waveform inversion in exploration geophysics. Geophysics 74(6):WCC1–WCC26

Walker AM, Wookey J (2012) Msat—a new toolkit for the analysis of elastic and seismic anisotropy. Comput Geosci 49:81–90

Wang S, Li XY, Qian Z, Di B, Wei J (2007) Physical modelling studies of 3-d p-wave seismic for fracture detection. Geophys J Int 168(2):745–756

Wang Z (2002) Seismic anisotropy in sedimentary rocks, part 2: Laboratory data. Geophysics 67(5):1423–1440

Warpinski NR, Waltman CK, Du J, Ma Q, et al (2009) Anisotropy effects in microseismic monitoring. In: SPE Annual Technical Conference and Exhibition, Society of Petroleum Engineers

Wuestefeld A, Al-Harrasi O, Verdon JP, Wookey J, Kendall JM (2010) A strategy for automated analysis of passive microseismic data to image seismic anisotropy and fracture characteristics. Geophys Prospect 58(5):755–773

Xu Y (2012) Analysis of p-wave seismic response for fracture detection: Modelling and case studies. PhD thesis, The University of Edinburgh

Xuan R, Sava P (2010) Probabilistic microearthquake location for reservoir monitoring. Geophysics 75(3):MA9–MA26

Yan B, Yuan S, Wang S, OuYang Y, Wang T, Shi P (2016) Improved eigenvalue-based coherence algorithm with dip scanning. Geophysics 82(2):V95–V103

Yomogida K, Etgen JT (1993) 3-d wave propagation in the los angeles basin for the whittier-narrows earthquake. Bull Seismol Soc Am 83(5):1325–1344

Yuan S, Wang S, Sun W, Miao L, Li Z (2014) Perfectly matched layer on curvilinear grid for the second-order seismic acoustic wave equation. Explor Geophys 45(2):94–104

Zhang JH, Yao ZX (2013) Optimized explicit finite-difference schemes for spatial derivatives using maximum norm. J Comput Phys 250:511–526

Zhang Y, Eisner L, Barker W, Mueller MC, Smith KL (2013) Effective anisotropic velocity model from surface monitoring of microseismic events. Geophys Prospect 61(5):919–930

Zienkiewicz OC, Taylor RL, Taylor RL (1977) The finite element method, vol 3. McGraw-hill London

Table 1 Memory cost for storing elastic parameters (including density of the medium) of different types of medium. M represents the model size

Medium type	Memory cost
Isotropic	3M
VTI/HTI	6M
Orthorhombic/TTI	10M
Monoclinic	14M
General anisotropic	22M

Table 2 Elastic parameters of layered medium

Layer	Thickness (m)	Vp (m/s)	Vs (m/s)	Density (kg/m^3)
1	750	3724	1944	2450
2	1000	4640	2583	2490
3	750	5854	3251	2680

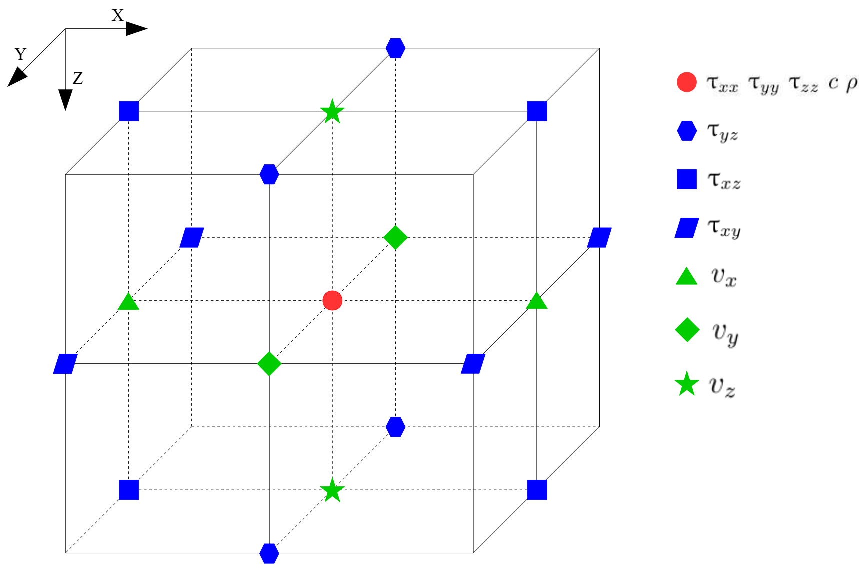

Fig. 1 Schematic representation of standard staggered-grid. v_x, v_y, v_z represent the particle velocity components along x-, y- and z-directions respectively; $\tau_{xx}, \tau_{yy}, \tau_{zz}, \tau_{yz}, \tau_{xz}, \tau_{xy}$ represent six components of the stress tensor; c and ρ represent the elastic tensor and density of the media

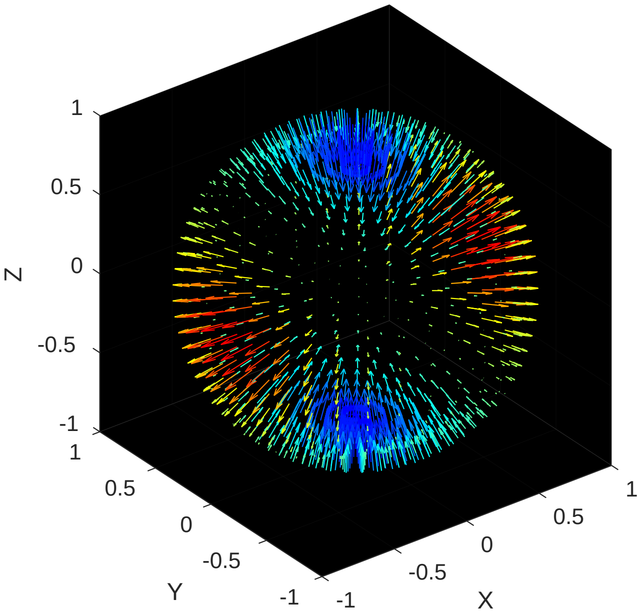

(a)

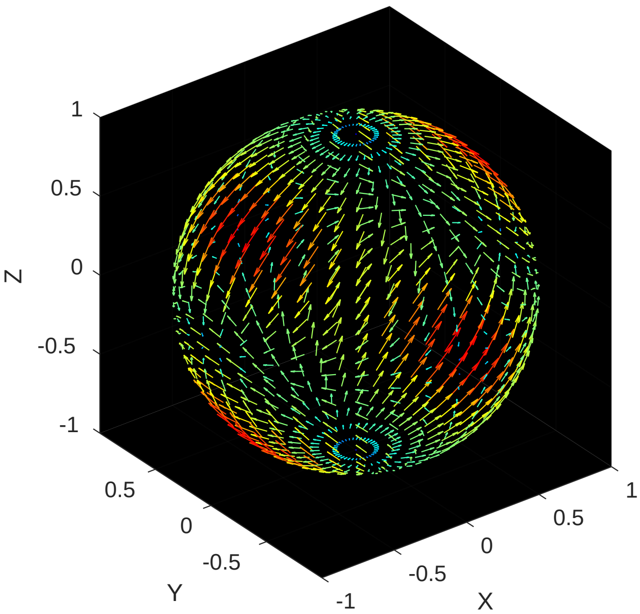

(b)

Fig. 2 P-wave (a) and S-wave (b) radiation patterns of a double-couple source in the far-field

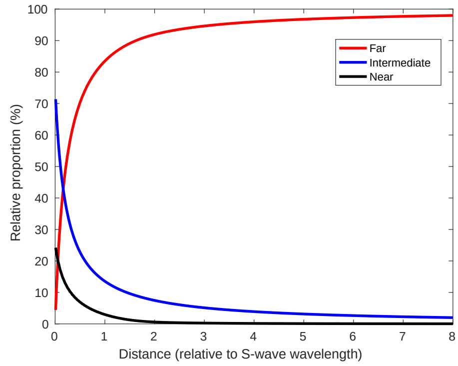

(a)

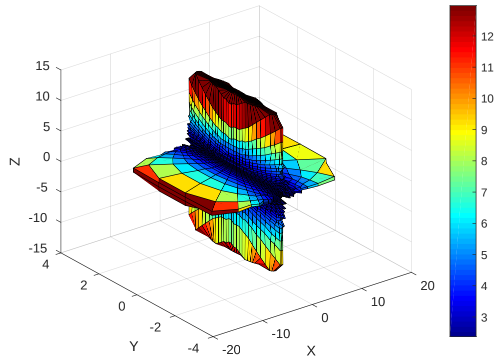

(b)

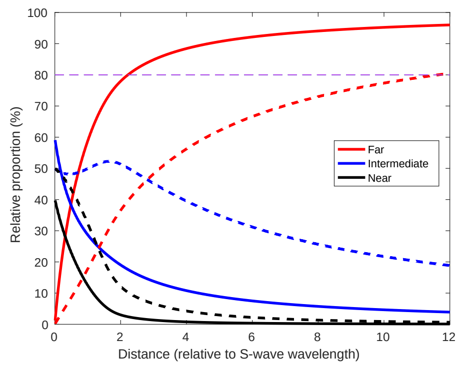

(c)

Fig. 3 (a) Relative magnitude of peak amplitude of the proportional part for near-field term, intermediate-field terms and far-field terms under certain parameters. (b) 3D map which shows the far-field distance in terms of S-wave wavelength in different directions for a double couple source. Beyond this far-filed distance, the far-field terms will occupy more than 80% energy in the whole wavefield. (c) Relative magnitude of wavefields for near-field term, intermediate-field S-wave term and far-field S-wave term for a double-couple source in different directions. The solid lines show the scenario in direction which has a zenith angle of 45° and azimuth angle of 0°. The dashed lines show the scenario in direction which has a zenith angle of 5° and azimuth angle of 0°

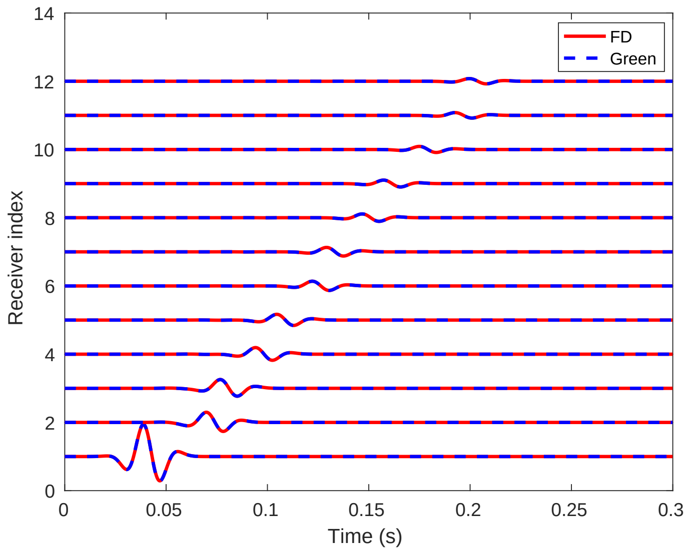

(a)

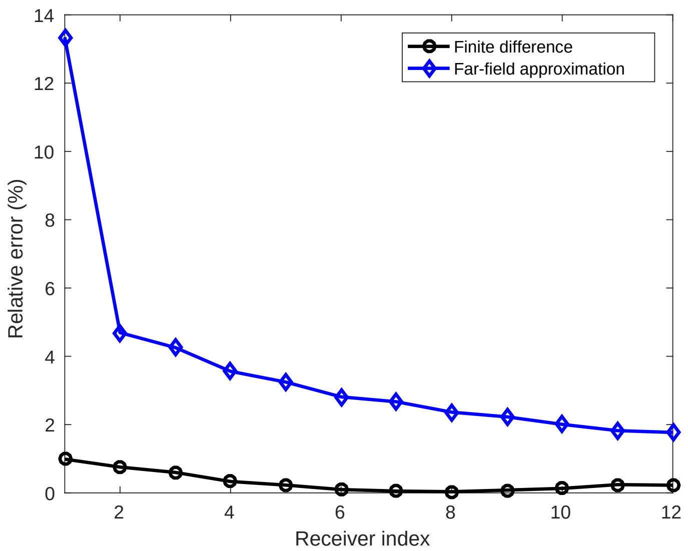

(b)

Fig. 4 (a) Synthetic seismograms (displacement in Y direction only) recorded by twelve receivers deployed in different directions and positions, with the FD results in solid red line overlaying the analytical solutions obtained by Green's function in dashed blue line. (b) Relative error of the peak amplitude of FD modeling and far-field approximation with respect to analytical solutions for the twelve FD records, with FD method in dark line and far-field approximation in blue line

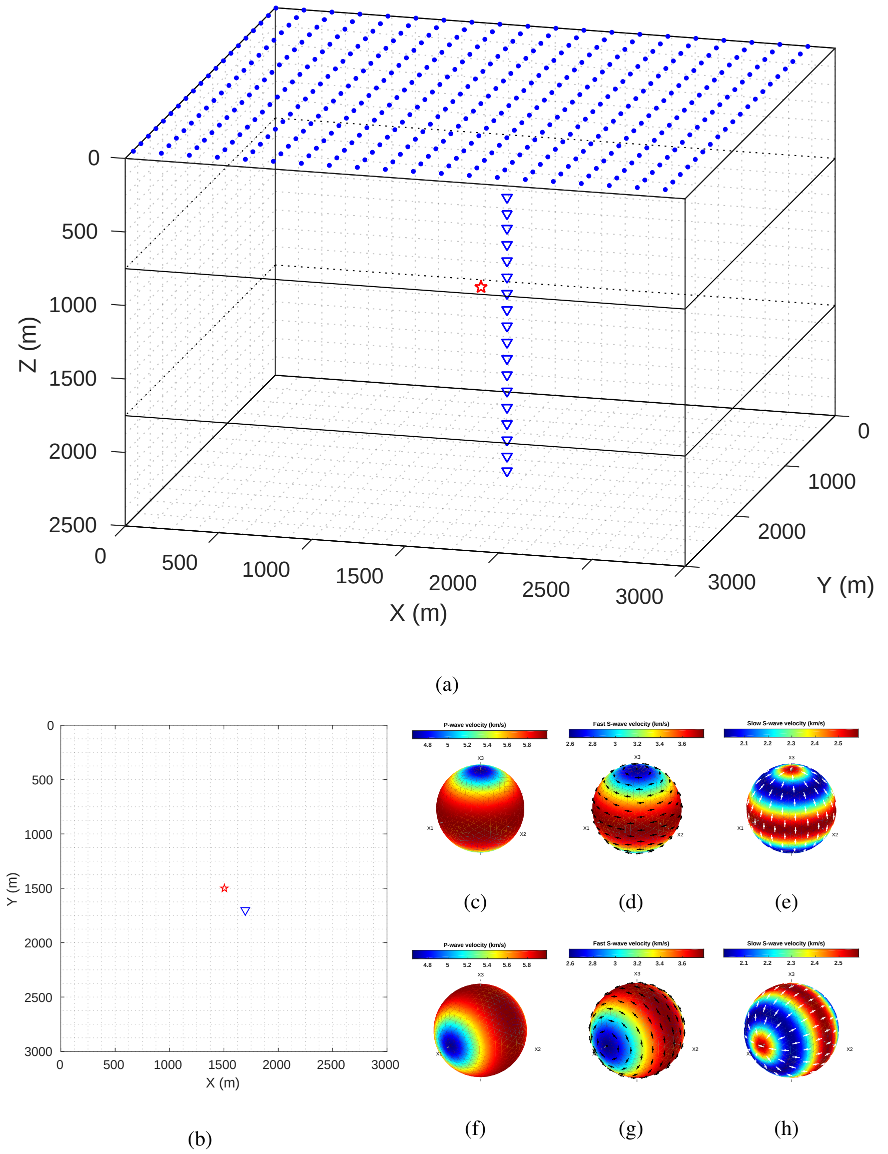

(a)

(b) (c) (d) (e) (f) (g) (h)

Fig. 5 (a) Schematic representation of the layered model and the recording arrays. The red star represents microseismic source, the blue points represent surface arrays, the blue triangles represent downhole arrays. The microseismic source is placed in the middle of the model. (b) Surface projection of the source and downhole array. Variation of the (c) P-wave, (d) fast S-wave and (e) slow S-wave velocity in VTI medium along different propagation directions. Variation of the (f) P-wave, (g) fast S-wave and (h) slow S-wave velocity in HTI medium along different propagation directions. The black and white markers indicate the fast and slow S-wave polarization directions, respectively

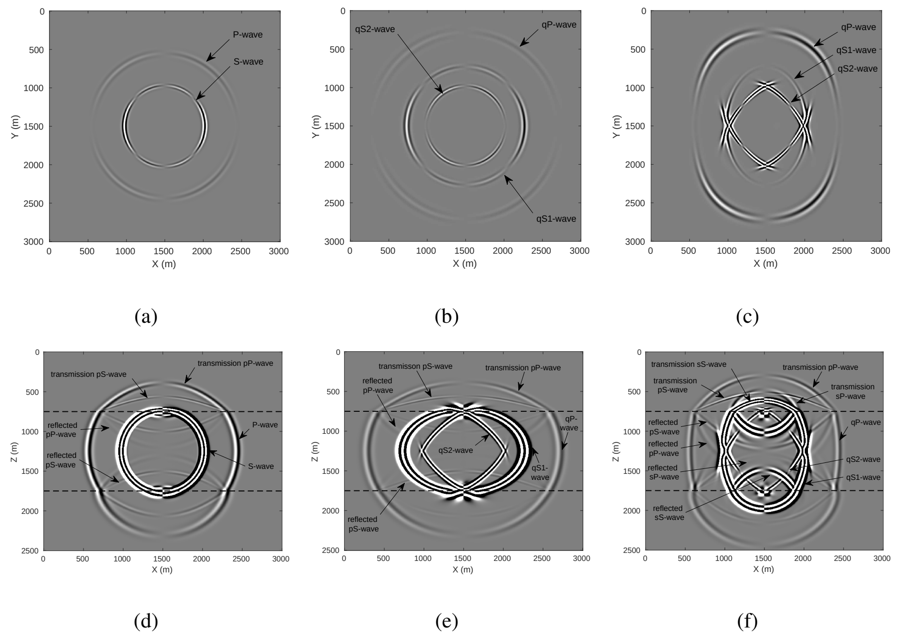

Fig. 6 Horizontal slices of velocity component in Y direction for the (a) isotropic, (b) VTI and (c) HTI model. The horizontal slices are taken at time of 0.23 s and depth of z = 1250 m. Vertical slices of velocity component in Y direction for the (d) isotropic, (e) VTI and (f) HTI model. The vertical slices are taken at a time of 0.23 s and lateral position of y = 1500 m. Dashed lines show boundaries of different layers

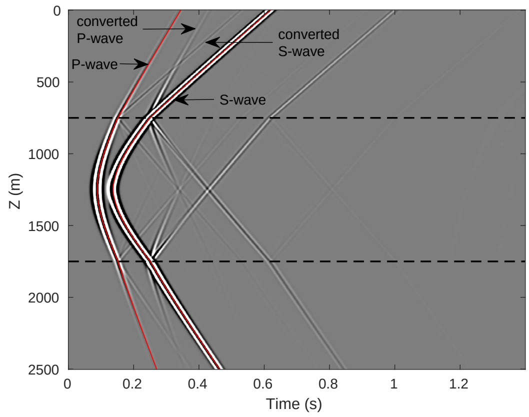

(a)

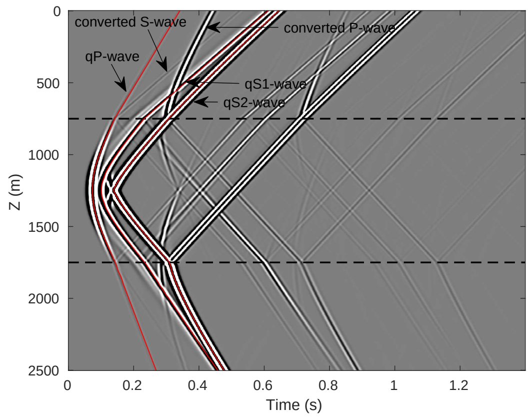

(b)

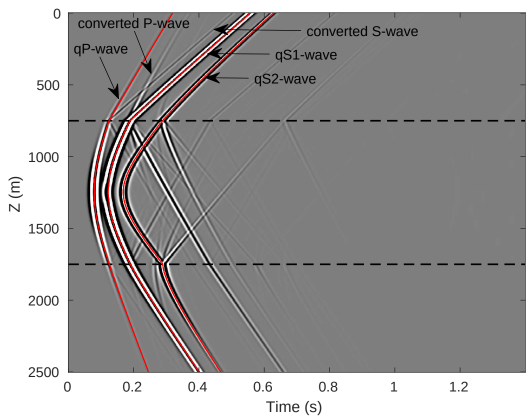

(c)

Fig. 7 The recorded seismograms in downhole array for the (a) isotropic, (b) VTI and (c) HTI model. Vertical axis shows the position of geophones and horizontal axis shows recording time. Red dotted lines represent the automatically picked direct P- and S-wave wavefronts; dashed lines show boundaries of different layers

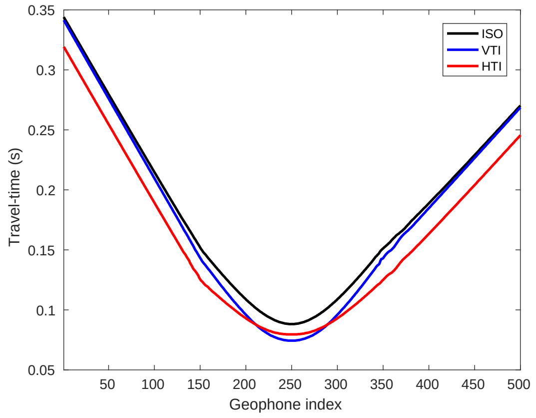

(a)

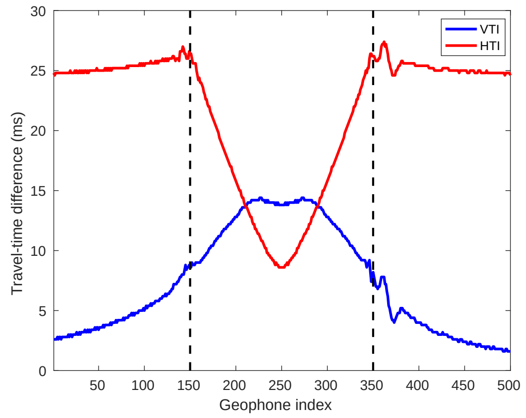

(b)

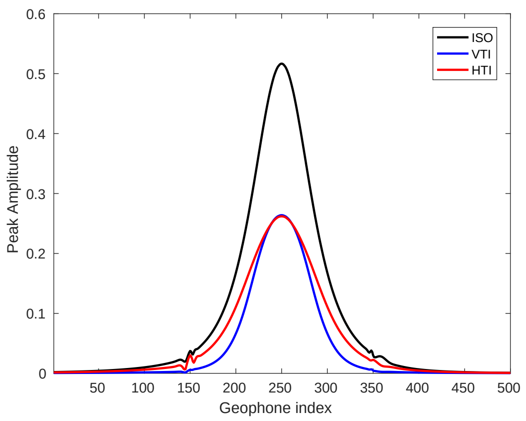

(c)

Fig. 8 Comparison of travel-times and peak amplitudes of the direct P-wave for three modelings. Dark solid line represents value in the isotropic model; blue solid line represents value in the VTI model; red solid line represents value in the HTI model; dashed lines show boundaries of the layers (geophone 150 and geophone 350 are placed at layer boundary, geophone 250 is at the same depth of microseismic source). (a) Travel-times of the direct P-wave. (b) Travel-time differences with respect to the isotropic case. (c) Peak amplitudes of the direct P-wave

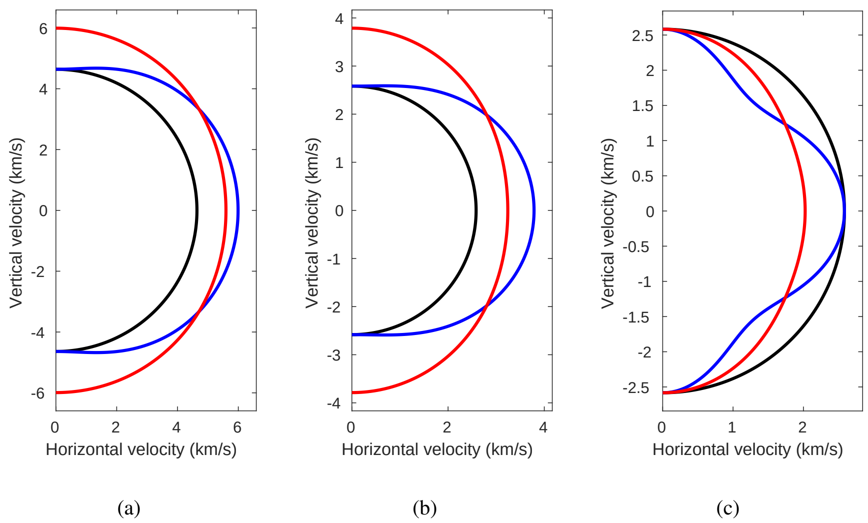

Fig. 9 Velocity surfaces of the P-, fast S- and slow S-waves, calculated in the same profile of the downhole array. The dark line represents the isotropic model; blue line represents the VTI model; red line represents the HTI model. For the isotropic model, there is only one S-wave mode, whose velocity is used in both fast and slow S-wave surface. (a) P-wave velocity surface; (b) fast S-wave velocity surface; (c) slow S-wave velocity surface

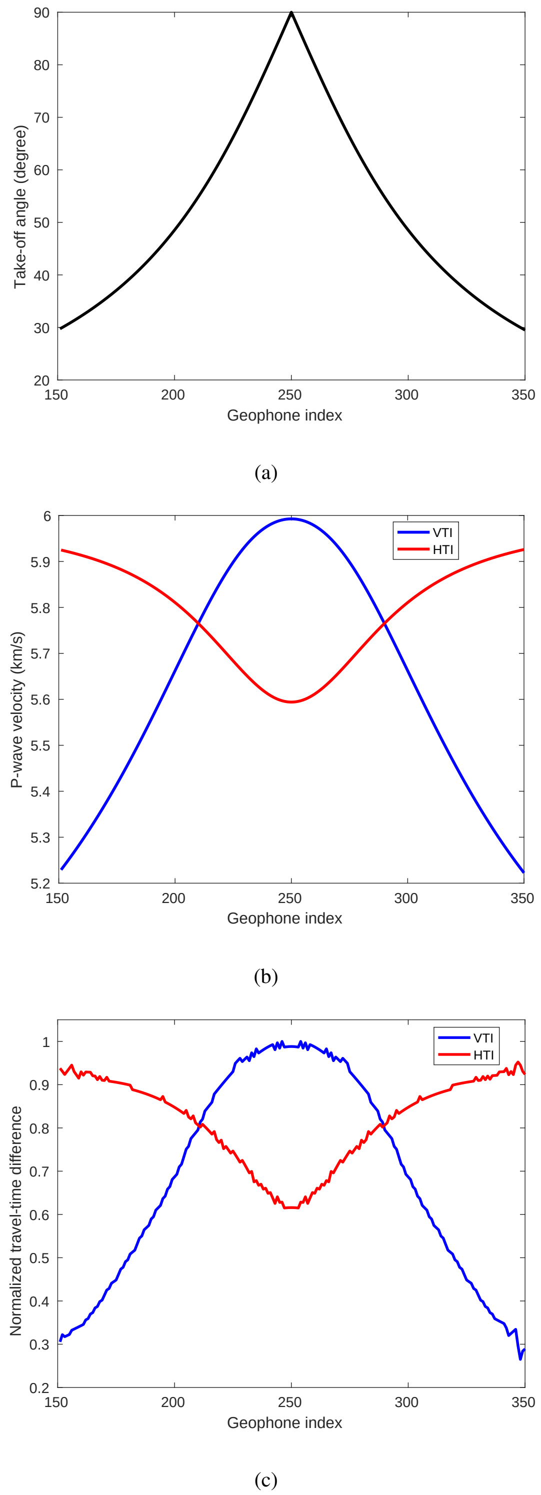

Fig. 10 (a) Relationship between the take-off angle and geophone index. (b) Velocity variation of the P-wave for downhole geophones at the second layer. (c) Normalized travel-time differences of the direct P-wave for downhole geophones at the second layer. The effect of the ray-path has been considered and eliminated

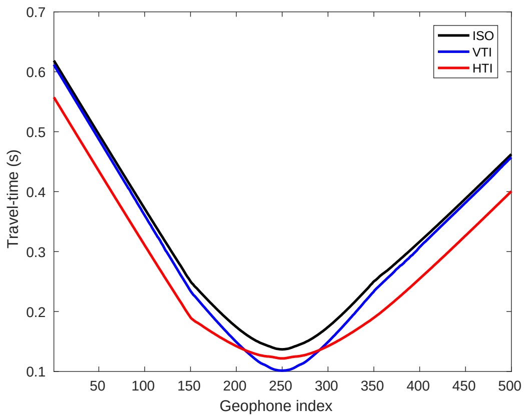

(a)

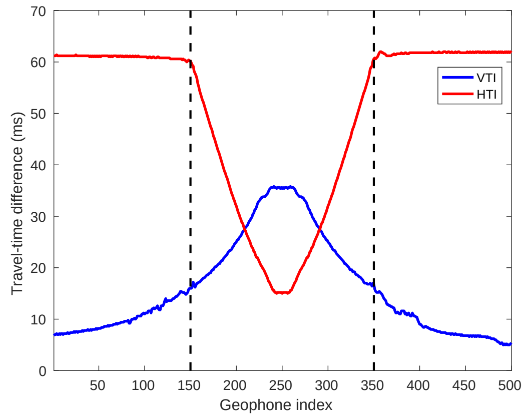

(b)

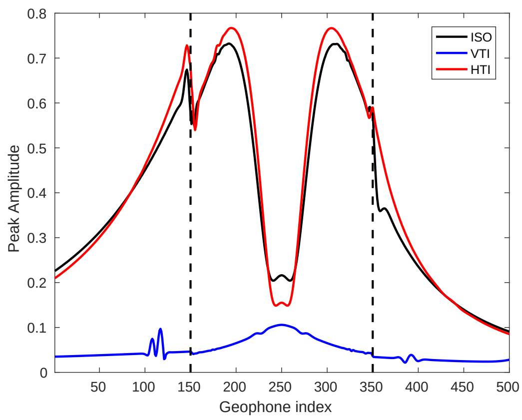

(c)

Fig. 11 Comparison of travel-times and peak amplitudes of the direct fast S-wave (S-wave in the isotropic case) for three modeling examples. The figure description is analogous to figure 8. The small wiggling in the figure are caused by picking error introduced by aliasing of different waves. The sudden jump of peak amplitudes near the layer boundaries is caused by sudden change in elastic parameters or wave impedance between layers. (a) Travel-times of the direct S-wave or fast S-wave. (b) Travel-time differences with respect to isotropic case. (c) Peak amplitudes of the direct S-wave or fast S-wave

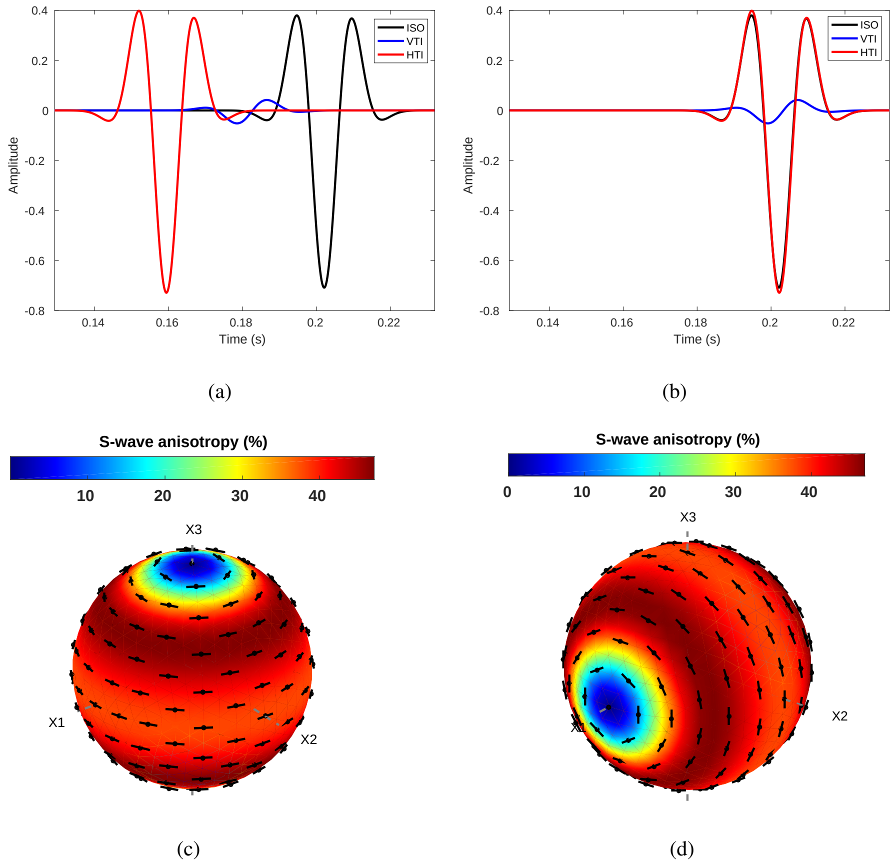

Fig. 12 Waveform of the direct fast S-wave (S-wave in isotropic case) before (a) and after (b) time alignment at downhole geophone 180. Variation of S-wave anisotropy along different propagation directions in the (c) VTI and (d) HTI medium

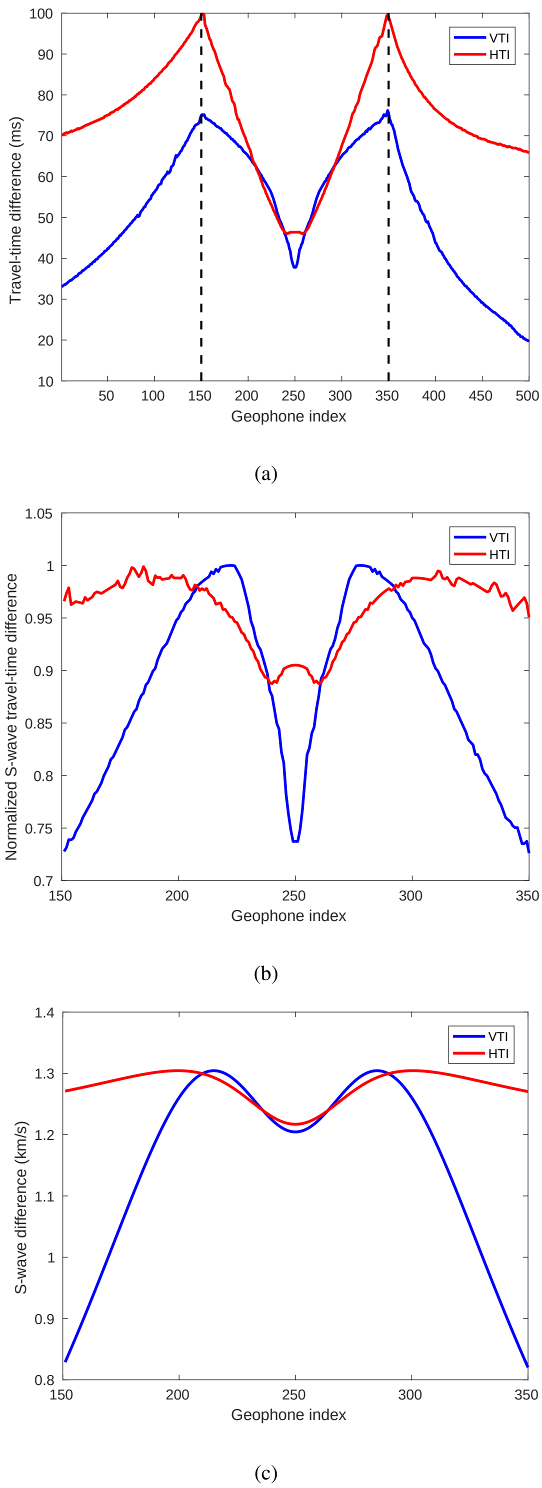

Fig. 13 (a) Travel-time differences between the fast S-wave and slow S-wave in the VTI and HTI model. (b) Normalized travel-time differences between the fast S-wave and slow S-wave in the VTI and HTI model at the second layer. The effect of the ray-path has been considered and eliminated. (c) Velocity difference between the fast S-wave and slow S-wave in the VTI and HTI model at the second layer

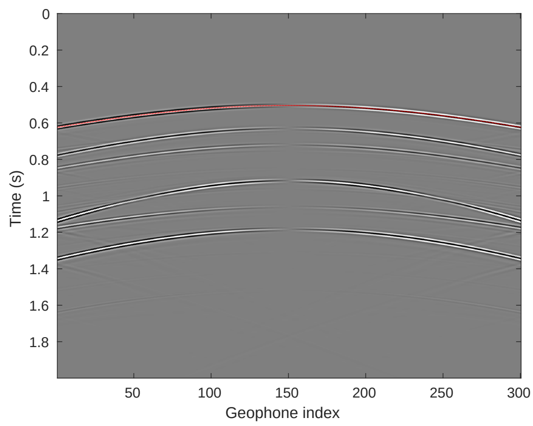

(a)

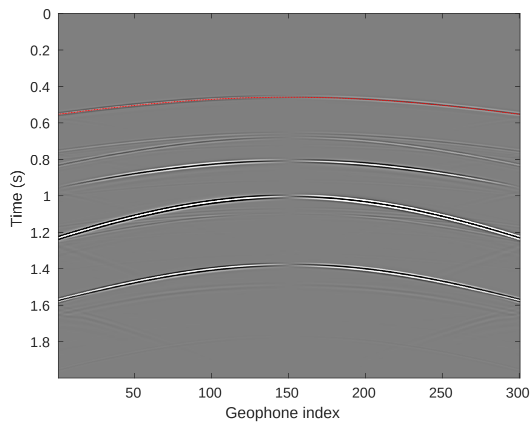

(b)

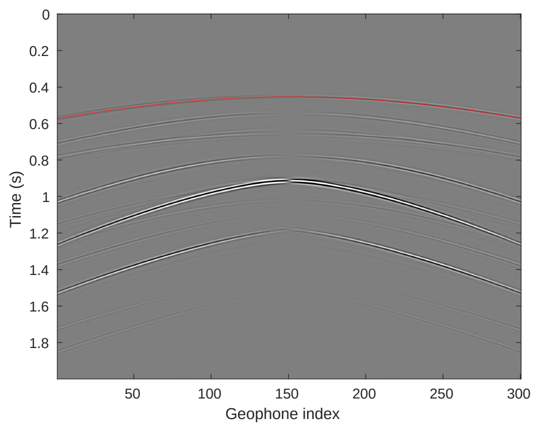

(c)

Fig. 14 Recorded seismic profiles for the (a) isotropic, (b) VTI and (c) HTI models using surface array. These profiles are recorded at the first receiver line in Y direction. The direct P-wave has been automatically picked and annotated with red line in the figure

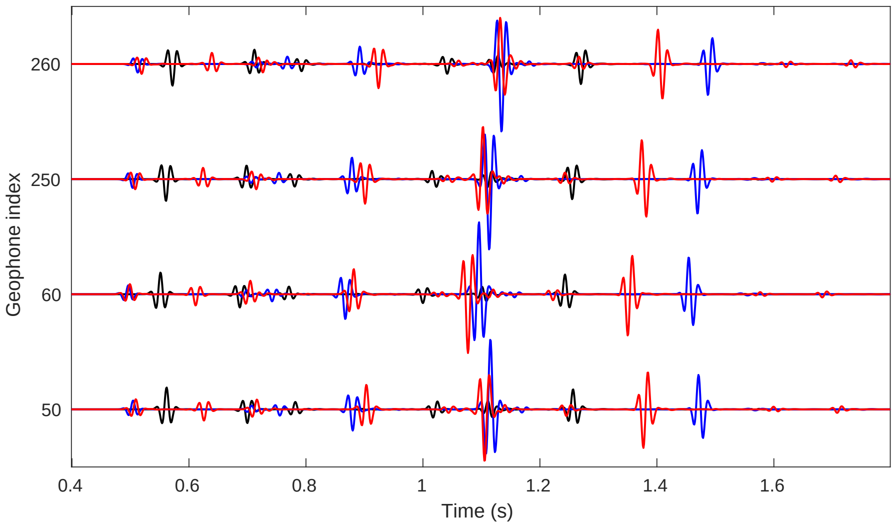

Fig. 15 Shown are four traces extracted form figure 14 with the isotropic case in dark line, the VTI case in blue line and the HTI case in red line

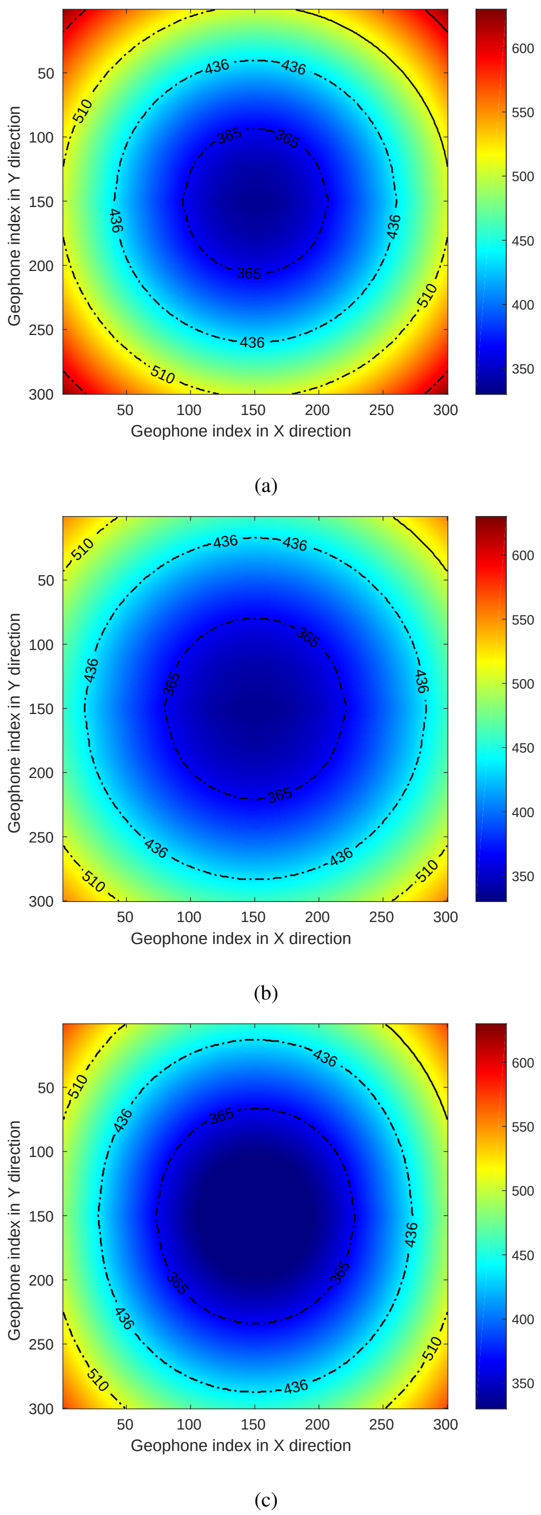

Fig. 16 Travel-times of the direct P-wave in the (a) isotropic, (b) VTI and (c) HTI models for the surface array. The unit of time in these figures is millisecond. The contour lines of travel-times are also displayed in the figure

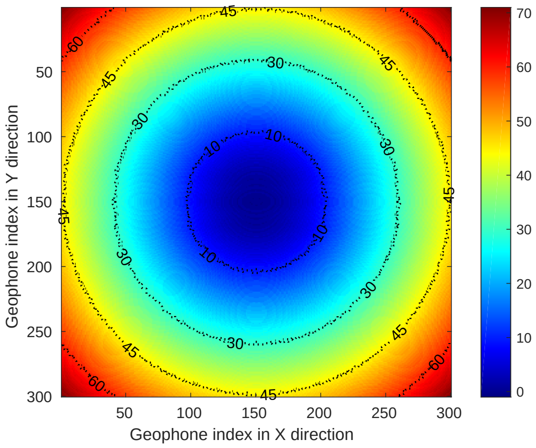

(a)

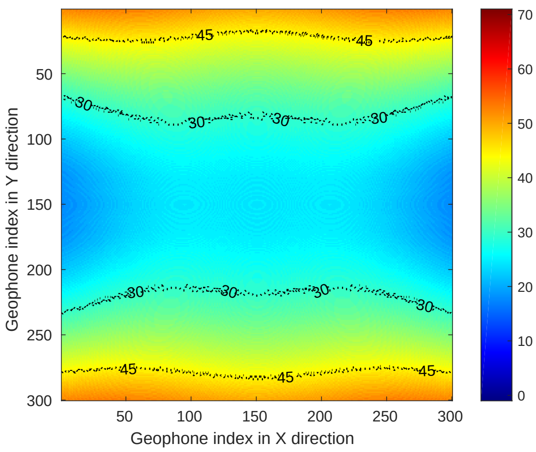

(b)

Fig. 17 Travel-time differences of the direct P-wave with respect to the isotropic case. (a) VTI model; (b) HTI model

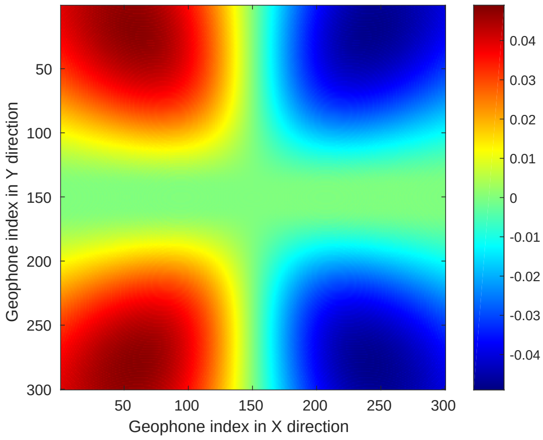

(a)

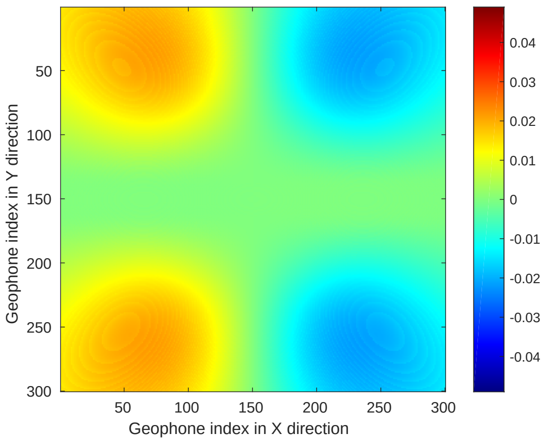

(b)

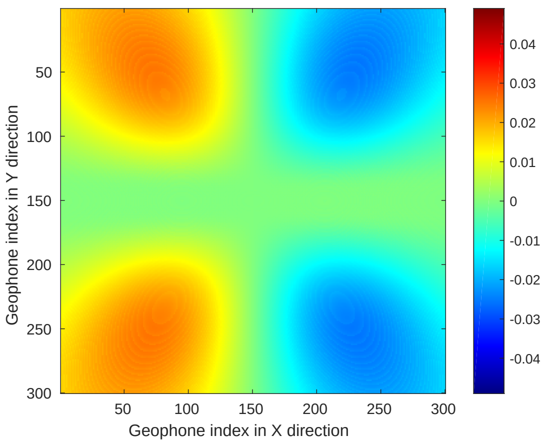

(c)

Fig. 18 Peak amplitudes of the direct P-wave in the (a) isotropic, (b) VTI and (c) HTI models for the surface array

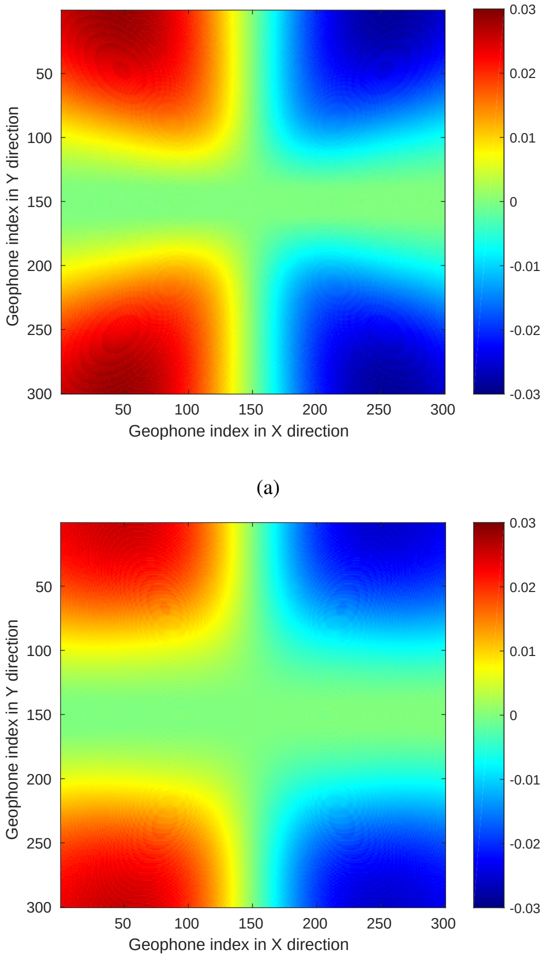

(a)

(b)

Fig. 19 Peak amplitude differences of the direct P-wave with respect to the isotropic case. (a) VTI model; (b) HTI model

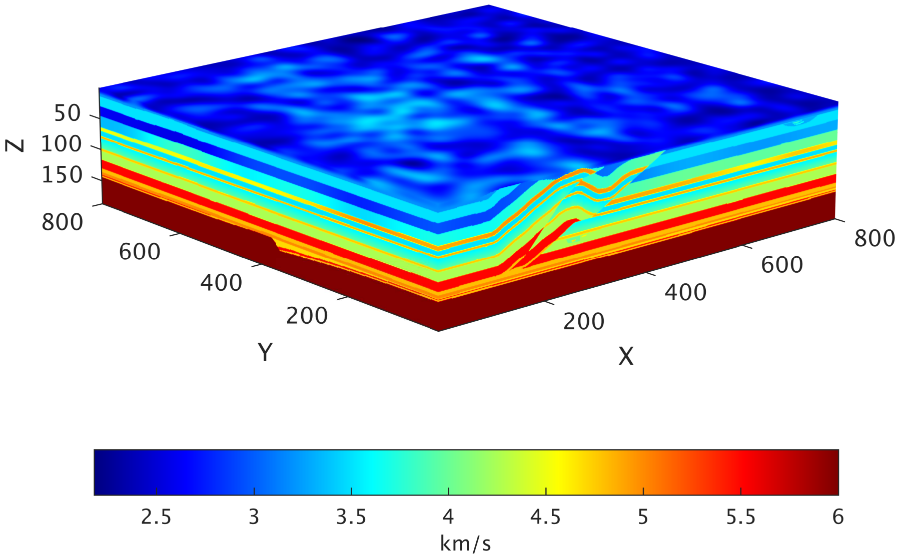

Fig. 20 P-wave velocity of the 3D overthrust model

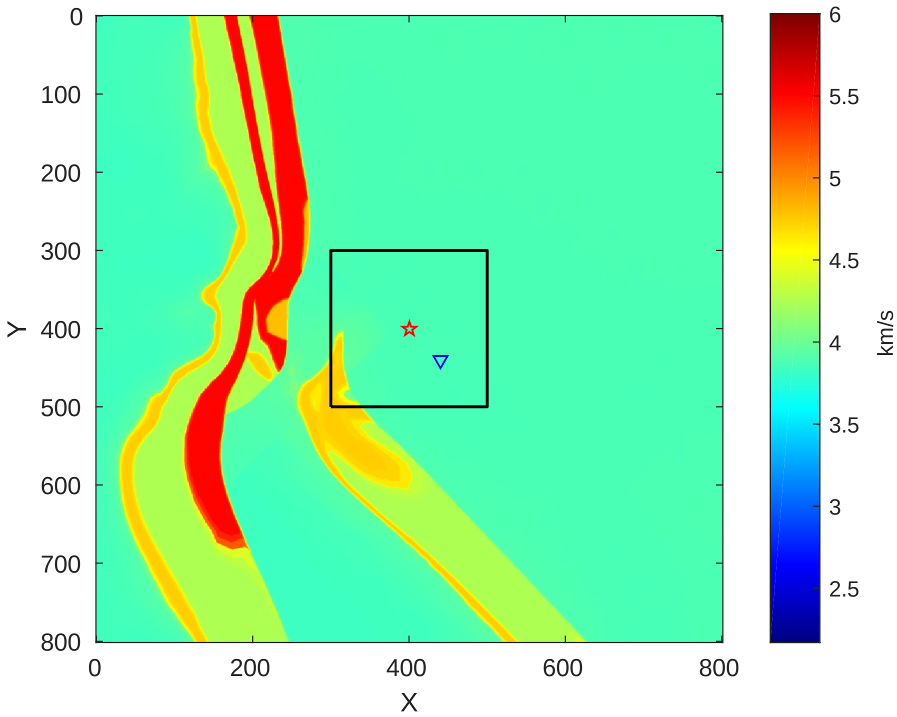

(a)

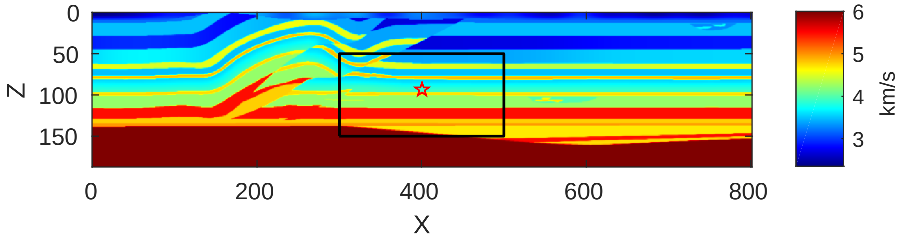

(b)

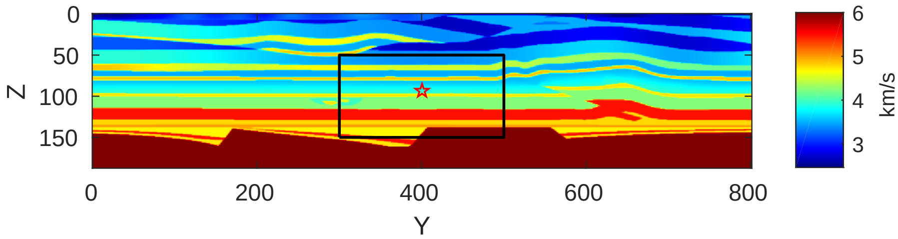

(c)

Fig. 21 Shown are P-wave velocity profiles of the 3D overthrust model. The red star represents source position; the black line exhibits the anisotropic region in the model; the blue triangle represents the horizontal projection of the vertical downhole array. (a) Velocity profile at index 93 of Z-axis. (b) Velocity profile at index 400 of Y-axis. (c) Velocity profile at index 400 of X-axis

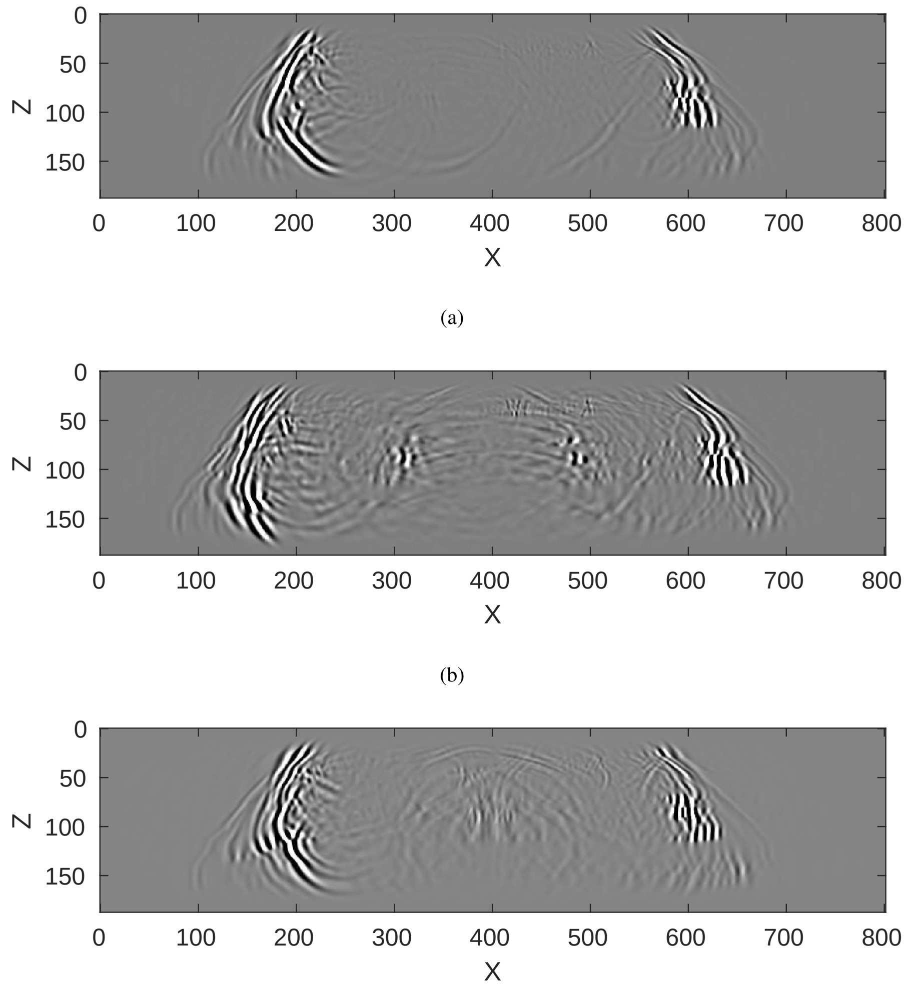

(a)

(b)

(c)

Fig. 22 Wavefield snapshots of velocity component in Y direction at 0.49 s and y = 400. (a) Isotropic case. (b) VTI case. (c) HTI case

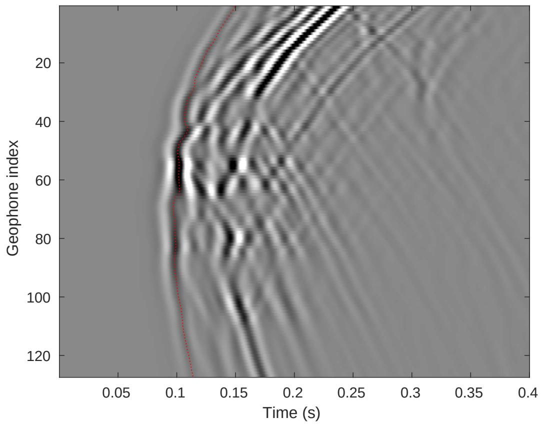

(a)

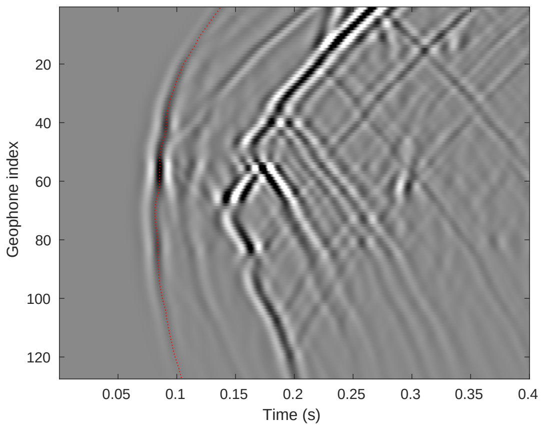

(b)

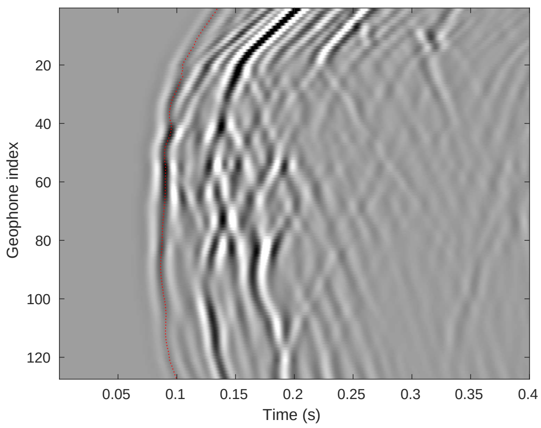

(c)

Fig. 23 The recorded seismograms in the downhole array for the (a) isotropic, (b) VTI and (c) HTI model. Red dotted lines represent the automatically picked direct P-wave wavefronts

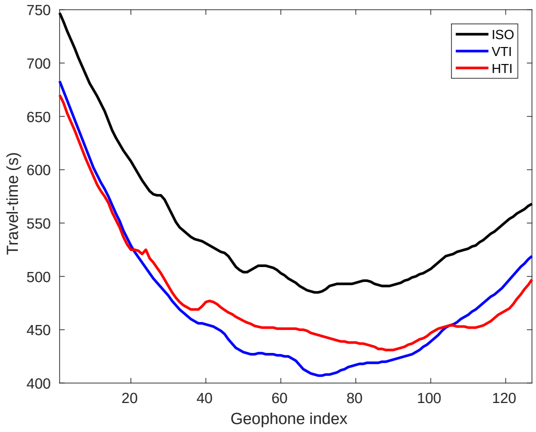

(a)

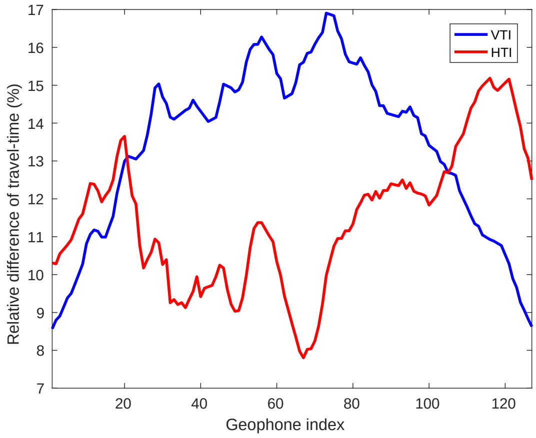

(b)

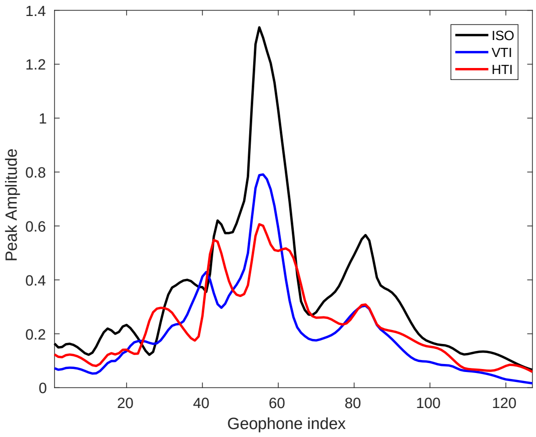

(c)

Fig. 24 Comparisons of travel-times and peak amplitudes of the direct P-wave for the isotropic, VTI and HTI model. Dark solid line represents value in the isotropic model; blue solid line represents value in the VTI model; red solid line represents value in the HTI model. (a) Travel-times of the direct P-wave. (b) Relative travel-time differences of the VTI and HTI model with respect to the isotropic model. (c) Peak amplitudes of the direct P-wave

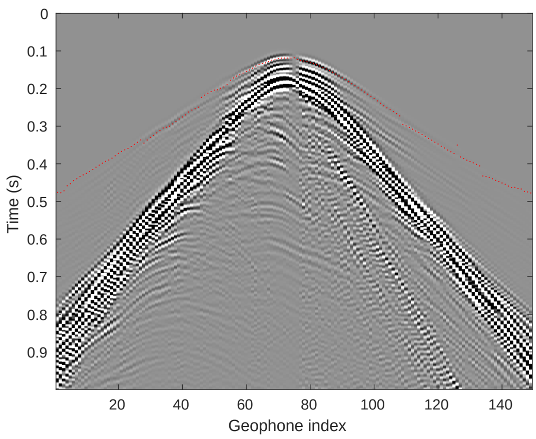

(a)

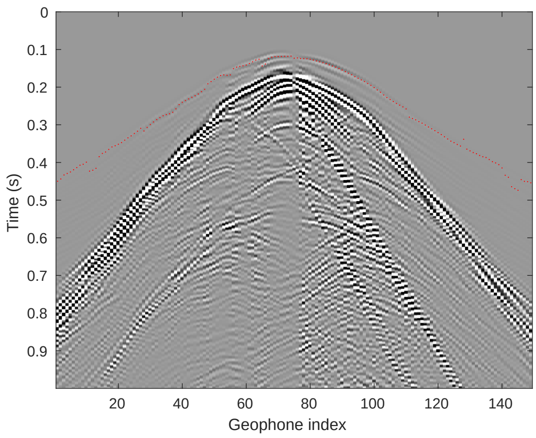

(b)

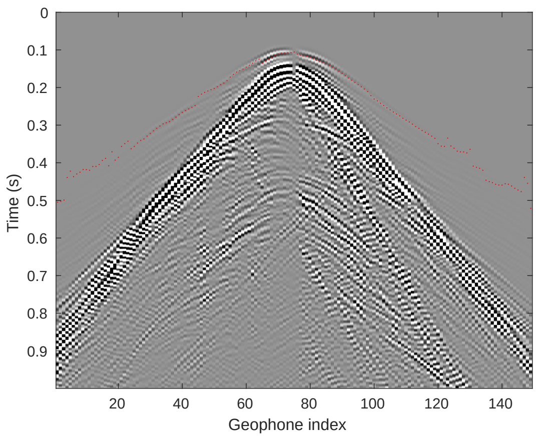

(c)

Fig. 25 The recorded seismic profiles in the surface array for the (a) isotropic, (b) VTI and (c) HTI model at the 70st receiver line in Y direction. Red dotted lines represent the automatically picked direct P-wave wavefronts

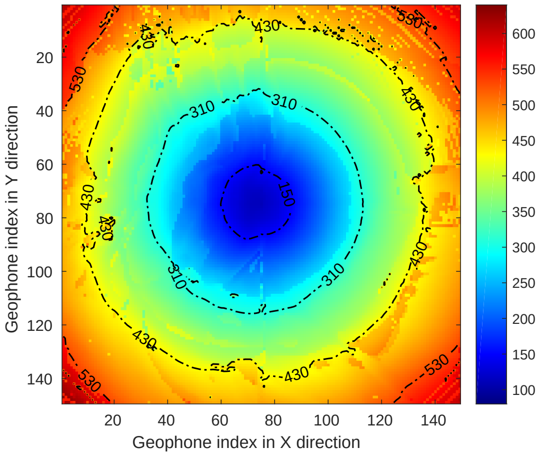

(a)

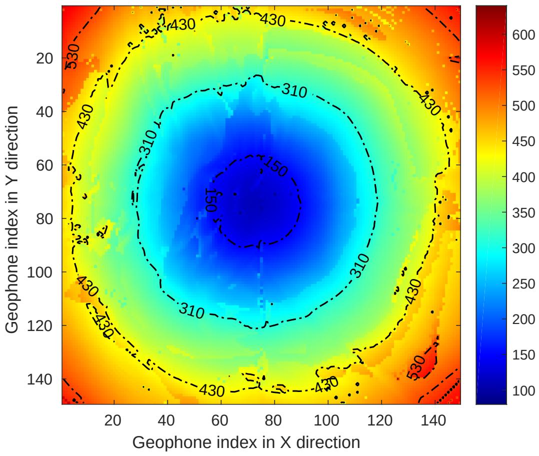

(b)

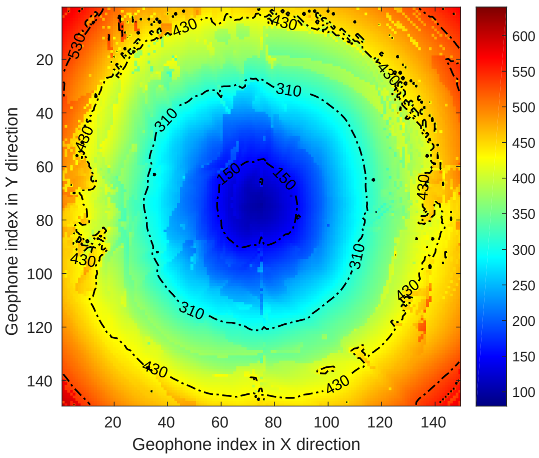

(c)

Fig. 26 Travel-times of the direct P-wave in the (a) isotropic, (b) VTI and (c) HTI model for the surface array. The contour lines of travel-times are also displayed in the figure. The unit of time in these figures is millisecond

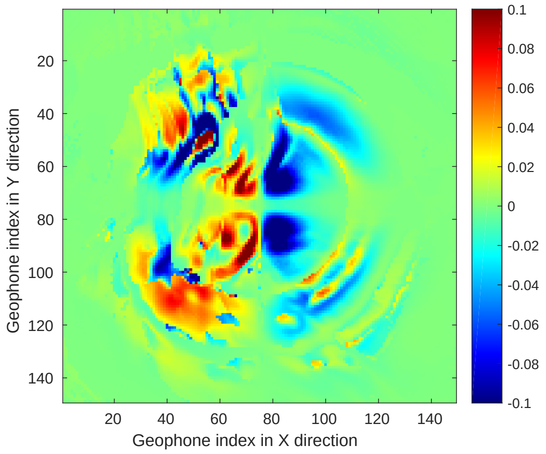

(a)

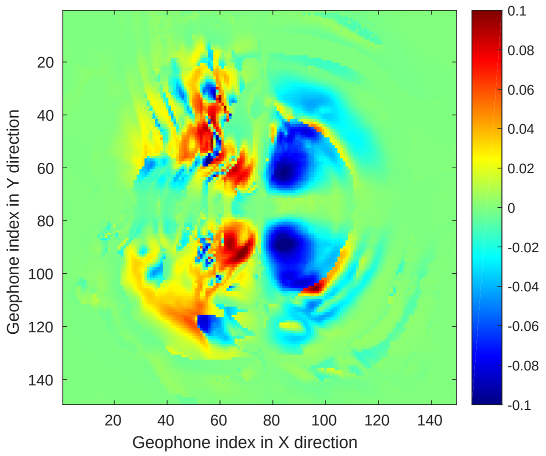

(b)

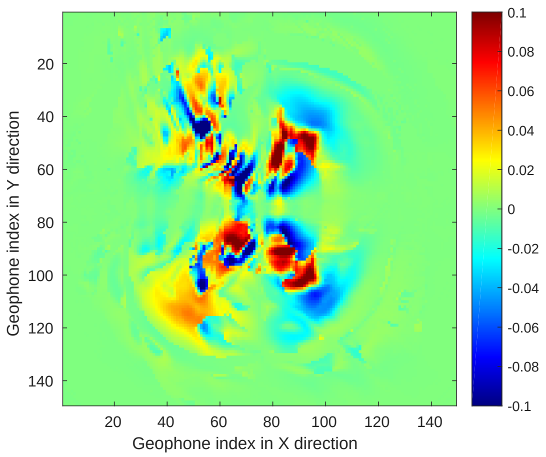

(c)

Fig. 27 Peak amplitudes of the direct P-wave in the (a) isotropic, (b) VTI and (c) HTI model for the surface array